

THERMAL NEUTRON SCATTERING EVALUATION FRAMEWORK

A Dissertation
Presented to
The Academic Faculty

by

Chris W. Chapman

In Partial Fulfillment
of the Requirements for the Degree
Doctor of Philosophy in Nuclear and Radiological Engineering in the
George W. Woodruff School of Mechanical Engineering

Georgia Institute of Technology
August 2017

COPYRIGHT © 2017 BY CHRIS W. CHAPMAN

THERMAL NEUTRON SCATTERING EVALUATION FRAMEWORK

Approved by:

Dr. Farzad Rahnema, Advisor
George W. Woodruff School
Georgia Institute of Technology

Dr. Bojan Petrovic
George W. Woodruff School
Georgia Institute of Technology

Dr. Goran Arbanas
Nuclear Data & Criticality Safety
Oak Ridge National Laboratory

Dr. Tom Morley
School of Mathematics
Georgia Institute of Technology

Dr. Dingkang Zhang
George W. Woodruff School
Georgia Institute of Technology

Dr. Mike Dunn
Director of Nuclear Services
Spectra Tech, Inc.

Date Approved: [June 23, 2017]

It was a very poor and inefficient way of producing energy, and anyone who looked for a source of power in the transformation of the atoms was talking moonshine – Ernest

Rutherford, 1932

ACKNOWLEDGEMENTS

First I would like to thank my advisor Dr. Farzad Rahnema for giving me a chance to work and study at Georgia Tech. Under his tutelage, I have learned so much about the field of nuclear engineering both from an industry as well as academic perspective. His guidance and helpful critique of my work has been critical in forming me into the student I am today. I would also like to thank Dr. Goran Arbanas for allowing me to work with him at the Oak Ridge National Laboratory. His patience and encouragement played a large role in the completion of this work, and I am certain that I could not have done it without his help.

I would also like to thank the rest of my committee, Dr. Bojan Petrovic, Dr. Dingkang Zhang, Dr. Tom Morley, and Dr. Mike Dunn, for agreeing to be on my committee, providing guidance and critique of my Ph.D. work. I would also like to thank Dr. Luiz Leal, who is predominantly the reason why this project exists, and who has provided constant support and encouragement throughout. I also want to acknowledge Dr. Jose Ignacio Marquez Damian, Vaibhev Jaiswal, Carl Wendorff and Kemal Ramic. Each of these wonderful scholars have helped me in my quest in completing this seemingly insurmountable task with their wisdom, technical expertise, and I look forward to working with them in the future.

During my extended tenure at Georgia Tech, my CRMPL lab mates did everything in their power to make the toil and turmoil of graduate school a bit more bearable. Specifically, Kevin Connolly, Ryan Hon, Alex Huning, Daniel Lago, Drew Johnson,

Gave Kooreman, Kyle Remley, Stefano Terlizzi, and Saam Yasseri, I sincerely thank you for keeping me on the path towards graduation.

I would not be the person I am today if it weren't for my family and friends. Specifically, my parents, Robin and Gary Chapman, and my friends from high school and Texas A&M have changed me in so many ways, most of which were for the best.

Finally, without the loving support of my wonderful wife, Laura Chapman, I surely would have lost my mind. Her endless love and compassion have done more to keep me sane and level-headed than I ever thought possible. Thank you.

This work was funded by the US Department of Energy Nuclear Energy University Program, as well as the US Department of Energy Nuclear Criticality Safety Program. Without their financial support, this work could not have been carried out. This research used resources of the National Energy Research Scientific Computing Center, a DOE Office of Science User Facility supported by the Nuclear Data and Nuclear Theory Program, Office of Nuclear Physics, and Office of Science of the U.S. Department of Energy under Contract No. DE-AC02-05CH11231, as well as resources of the ORNL Institutional Cluster

TABLE OF CONTENTS

ACKNOWLEDGEMENTS	iv
LIST OF ABBREVIATIONS	viii
LIST OF TABLES	ix
LIST OF FIGURES	x
SUMMARY	xi
CHAPTER 1. Introduction	1
1.1 Thermal Scattering	1
1.2 Water	3
1.3 Motivation and Goals	4
CHAPTER 2. Theory	6
2.1 Thermal Scattering Cross Sections	6
2.1.1 Static Target	6
2.1.2 Non-Static Target	9
2.1.3 Fermi Pseudopotential	14
2.1.4 Time Domain	16
2.1.5 Coherent and Incoherent Scattering	19
2.1.6 Van Hove Theory	22
2.1.7 Gaussian Approximation	24
2.2 Unified Monte Carlo	25
2.2.1 UMC-G	27
2.2.2 UMC-B	28
2.3 Water Models	29
CHAPTER 3. Framework Overview & Results	35
3.1 Experimental Data	35
3.2 Framework	36
3.3 Results	41
3.3.1 TIP4P/2005f Parameters and Properties	41
3.3.2 Double Differential Cross Section	49
3.3.3 Total Cross Section	53
CHAPTER 4. Benchmarks	57
4.1 Benchmark Descriptions	58
4.1.1 PST-033-003	58
4.1.2 LCT-079-007	63
4.1.3 HCT-006-003	67
4.2 Benchmark Results	71
CHAPTER 5. Conclusion and Future Work	77

APPENDIX A Double Differential Cross Section Plots	79
REFERENCES	86

LIST OF ABBREVIATIONS

DDCS	Double Differential Cross Section
SNS	Spallation Neutron Source
ORNL	Oak Ridge National Laboratory
UMC	Unified Monte Carlo
MD	Molecular Dynamics
HEU	High Enriched Uranium
LEU	Low Enriched Uranium
PST	Plutonium Solution Thermal
LCT	LEU Composite Thermal
HCT	HEU Composite Thermal
DSF	Dynamic Structure Factor
ENDF	Evaluated Nuclear Data File
CAB	Center Atómico Bariloche
IKE	Institut für Kernenergetik und Energiesysteme

LIST OF TABLES

Table 1. Published TIP4P/2005f parameters	37
Table 2. TIP4P/2005f parameters – First Iteration	41
Table 3. Results of UMC on TIP4P parameters	42
Table 4. Correlation Matrix of TIP4P Parameters from UMC	45
Table 5. Result of UMC analysis on various properties	46
Table 6. Properties from TIP4P/2005f potential at 298 K	47
Table 7. Material Specifications for PST-033-003	62
Table 8. Material Specifications for LCT-079-007	66
Table 9. Material Specifications for HCT-006-003	70
Table 10. PST-033-003 Results	72
Table 11. LCT-079-007 Results	73
Table 12. HCT-006-003 Results	74

LIST OF FIGURES

Figure 1. Energy groupings demonstrated on ^{235}U	2
Figure 2: Diagram of Neutron Scattering Experiment.....	7
Figure 3. 4-Site Water Molecule.....	30
Figure 4. Lennard-Jones Potential	32
Figure 5. Comparison of bond potentials.....	34
Figure 6. Distribution of TIP4P/2005f parameters. The red line is the value originally reported in Table 2.	44
Figure 7. Distribution of properties.	48
Figure 8: DDCS plot with incident energy of 151 meV and scattering angles between 15° - 145°	51
Figure 9: DDCS plot with incident energy of 304 meV and scattering angles between 15° - 125°	52
Figure 10. Total cross section of light water for both methods of uncertainty generation.	54
Figure 11. Comparison of DSFs	56
Figure 12. Sensitivity plot of k_{eff} for ICSBEP benchmark problems.....	58
Figure 13. XZ view of the PST-033-003 benchmark. The numbers correspond to material labels detailed in Table 7.	60
Figure 14. XY view of the PST-033-003 benchmark. The numbers correspond to material labels detailed in Table 7.	61
Figure 15. XZ view of the LCT-079-007 benchmark. The material labels are left off for convenience, but the colors correspond to the materials detailed in Table 8.	64
Figure 16. XY view of the LCT-079-007 benchmark. The material labels are left off for convenience, but the colors correspond to the materials detailed in Table 8.	65
Figure 17. XZ view of the HCT-006-003 benchmark. The material labels are left off for convenience, but the colors correspond to the materials detailed in Table 9.	68
Figure 18 XY $1/4^{\text{th}}$ view of the HCT-006-003 benchmark. The material labels are left off for convenience, but the colors correspond to the materials detailed in Table 9.....	69
Figure 19. PST benchmark run for each accepted ensemble	75
Figure 20. LCT PST benchmark run for each accepted ensemble	75
Figure 21. HCT PST benchmark run for each accepted ensemble	76
Figure 22: SNS DDCS plots for $E_i=55$ meV	79
Figure 23: SNS DDCS plots for $E_i=160$ meV	80
Figure 24: SNS DDCS plots for $E_i=250$ meV	81
Figure 25: SNS DDCS plots for $E_i=600$ meV	82
Figure 26: SNS DDCS plots for $E_i=1000$ meV	83
Figure 27: SNS DDCS plots for $E_i=3000$ meV	84
Figure 28: SNS DDCS plots for $E_i=5000$ meV	85

SUMMARY

In this work, a thermal neutron scattering data evaluation framework is presented that combines measured scattering data and computer simulations to evaluate the dynamic structure factor (DSF), double differential cross section (DDCS), and their uncertainties. The original parameter set of a given interaction model is randomly sampled according to interaction parameters' prior probability distribution function. For each set of perturbed parameters, a corresponding DSF and DDCS are computed, and a weight associated with this set of perturbed parameters is obtained using a Unified Monte Carlo (UMC) method from the differences between simulated and measured data. Using these weights, the best estimate of the DSF and its uncertainty is computed as a weighted average of DSF values of all perturbed parameters sets. This is the first time thermal neutron scattering kernel uncertainties have been estimated by sampling the underlying atomic interaction model parameters.

This evaluation framework is demonstrated on the TIP4P/2005f light water interaction model combined with DDCS data measured at the Spallation Neutron Source (SNS) Fine Resolution Fermi-Chopper Spectrometer (SEQUOIA) at Oak Ridge National Laboratory (ORNL). Molecular dynamics trajectories computed from randomly sampled TIP4P/2005f parameters by the GROMACS code were processed to yield thermal neutron scattering kernel DSF and DDCS. An ensemble of 60 randomly perturbed TIP4P/2005f interaction parameters yielding satisfactory agreement with experimentally measured characteristics of light water were found. For each of these 60 parameter sets the UMC expressions were used to compute their associated weights based on the quality

of agreement between the corresponding DDCS and SNS data. These UMC weights were used to compute a weighted average of the DSF, the corresponding DDCS, and the total scattering cross section, as well as their corresponding uncertainties. The averaged cross sections computed from this DSF were then validated against independent experimental data (including DDCS and total cross section), as well as relevant benchmarks in the International Handbook of Evaluated Criticality Safety Benchmarks (ICSBEP), including the PU-SOL-THERM-033, LEU-COMP-THERM-079, and HEU-COMP-THERM-006 benchmarks. MCNP simulations of these integral benchmark experiments were performed for each DSF in the ensemble to produce a spread of neutron multiplication factors (k_{eff}) that represents a measure of uncertainty caused by uncertainty in the DSF for the first time.

CHAPTER 1. INTRODUCTION

There's an ideal in computer science that the accuracy of a computer simulation can only be as good as input data it is given. This theorem holds true for nuclear engineering as well in the form of cross section data. With the rise in fidelity of neutron transport codes, the primary source of uncertainty is moving away from uncertainties in the solution method of transport codes and shifting towards uncertainties in the nuclear data. This is especially concerning for thermal scattering cross section data specifically, as there are no available uncertainties in this energy region.

1.1 Thermal Scattering

Neutron cross sections can be categorized into three energy regions: thermal, epithermal, and fast. A schematic showing these energy regions is shown in Figure 1. The exact bounds between thermal, epithermal, and fast are debatable, but their general locations are shown in the plot. In the epithermal and fast energy regions, the neutron is energetic enough to render the vibrational energy of the target nucleus as well as the binding energies of a target molecule or crystalline structure as negligible. In the thermal region, however, the neutron energy is comparable to these vibrational and binding energies, meaning they must be considered when considering what the neutron cross section is at these energies.

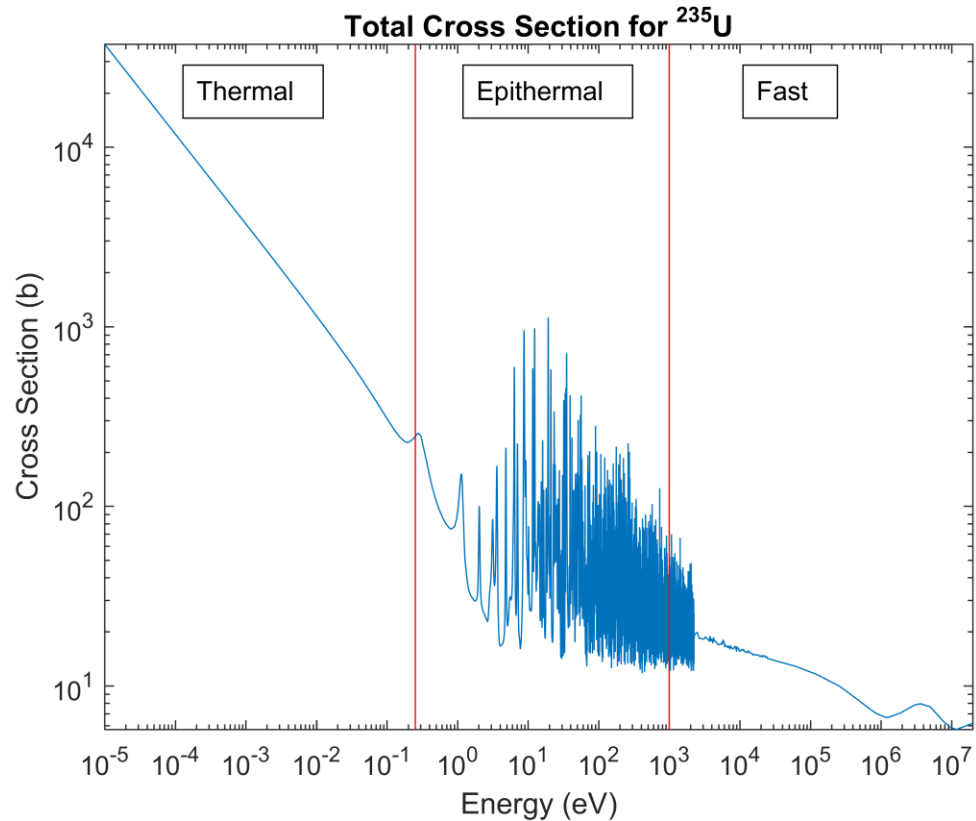


Figure 1. Energy groupings demonstrated on ^{235}U

As with epithermal and fast systems, the desire for accurate nuclear data for thermal systems is crucial [1]. With the rise in interest of GEN-IV reactor systems, specifically very high temperature and molten salt reactors, there has been a need for newer, more accurate thermal scattering data. In addition to GEN-IV reactors, current light water reactors that are applying for license extensions need high fidelity cross sections and uncertainties to better quantify whether they can operate safely for another 20 years. In addition, thermal moderator data plays a key role in nuclear criticality safety analyses. Currently, there are very limited thermal moderator data for materials that are of interest to nuclear criticality safety (e.g., Lucite, paraffin, hydrofluoric acid, etc.). The lack of uncertainties or covariance data for thermal scattering materials means that there is no

way of quantifying the effects of thermal scattering uncertainties in quantities of interest in reactor systems, though there have been recent efforts to try and quantify these covariances, [2]. Additionally, there currently does not exist a method for storing the uncertainties or covariances in the ENDF file format.

1.2 Water

Water is notoriously difficult to model computationally [3]. There currently exist more than 20 unique models that describe the location of the atoms in the molecule, the distribution of charge in the molecule, and how the molecule interacts with other molecules [4]. The earliest grouping of models is based on empirical data, meaning the models are non-polarizable, use point charges to represent electrostatic forces, and a Lennard-Jones potential for dispersion and repulsion. As computers became more powerful, water models were created to better characterize the polarization effects seen in water-water interactions. Finally, with the rise of *ab initio* method, highly detailed models of water can be generated for use in other *ab initio* code systems.

Attempts to determine the thermal scattering cross section of water analytically date back to the 1960's, when the first analytical model for the double differential cross section of water was developed by Nelkin [5]. This model made several assumptions, including: approximating the normal modes of motions in terms of torsional oscillations and translational motions of a rigid water molecule plus the internal vibrations of the molecule, replacing the hindered molecular rotation with a single torsional oscillation, and small collision times. The model was the basis of the ENDF/B-III evaluation of the thermal scattering of hydrogen in light water, where no attempt was made to estimate

uncertainties [6]. This evaluation was generated using the code GASKET, which improved on the Nelkin model by replacing the single torsional oscillator by a broad band of distributed modes.

No changes were made in the evaluation of the thermal scattering kernel of light water until 1994 with the release of ENDF/B-VI Release 2 [7], which kept much of the physical model from ENDF/B-III, but extended the α and β grids, which correspond to momentum and energy transfer, respectively. This new release was also evaluated using the LEAPR code, now found in NJOY [8]. This model was kept until 2006, when ENDF/B-VII was released. This evaluation was generated at Institute for Nuclear Technology and Energy Systems (IKE) [9] using NJOY, where the α and β grids were again extended and physical constants were updated to match more recent hydrogen and oxygen evaluations.

1.3 Motivation and Goals

This dissertation is motivated by the lack of thermal scattering data for various materials previously mentioned and the need to estimate their uncertainties. The recent improvements to the thermal scattering data for water made by the CAB model also shows that there is still room for development for ways to generate thermal scattering data [10]. The fact that many of the available thermal scattering data is generated using a variety of methods instead of a one-size-fits-all method is also a reason for investigation.

The goal of this dissertation is to provide a generalized framework for generating thermal scattering data and to validate this framework against available experimental data as well as experimental benchmarks to prove their improved results in real-world

applications. The expression for double differential thermal scattering cross sections and Unified Monte Carlo are derived in Chapter 2. The generalized framework, as well as results comparing these new cross sections against experimental data, is discussed in Chapter 3. Validation of these new cross sections using benchmark problems are presented in Chapter 4. Finally, conclusions and future work are given in Chapter 5.

CHAPTER 2. THEORY

For completeness, the full derivation of the double differential cross section from the beginnings of a simple scattering experiment will be outlined here. This derivation is detailed in several references [11] [12], and will be summarized below. Although this derivation is based on quantum mechanics, some approximations are made in order to use classical molecular dynamic atomic trajectories.

2.1 Thermal Scattering Cross Sections

2.1.1 *Static Target*

A thermal neutron scattering experiment can be described in the following way. Suppose a neutron of energy E_i , spin s_i , and momentum $\hbar\mathbf{k}_i$ is traveling towards a target as depicted below in Figure 2. The target is assumed to be static in this example, but it is not a required limitation.

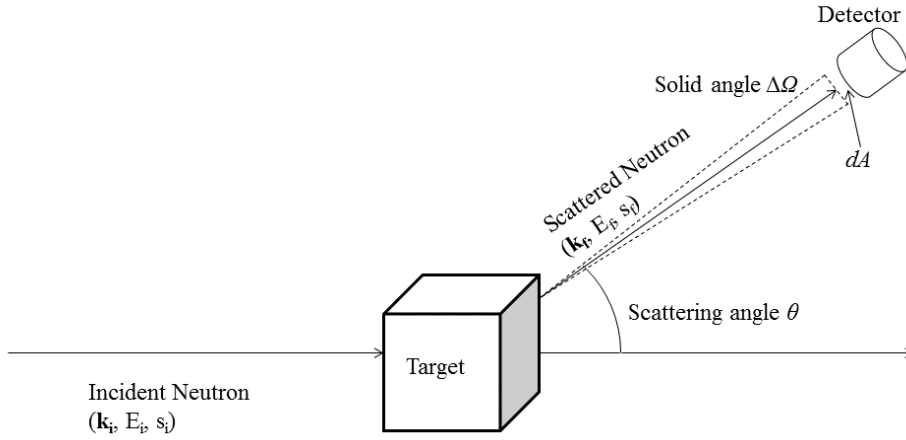


Figure 2: Diagram of Neutron Scattering Experiment

If the target is assumed to remain static during the experiment, then the number of neutrons (or the count C) that hit the detector can be defined as

$$C = \eta\Phi N \frac{d\sigma}{d\Omega} \Delta\Omega, \quad (2.1)$$

where η is the detector resolution, Φ is the neutrons crossing per unit area per unit time (also called the incident flux of neutrons), N is the number of atoms in the target, and $d\sigma/d\Omega$ is the differential scattering cross section with respect to angle. This assumes a single scattering event occurs in the target. The energy dependence of the cross section will be taken into consideration later.

The next step is to write out what the incident and scattering wavefunctions are. Since the energies of interest are on the order of several meV, the corresponding neutron wavelength is on the order of 10^{-10} m, as shown below

$$E = \frac{\hbar^2}{2m\lambda^2} \rightarrow \lambda = \frac{\sqrt{2mE}}{\hbar}, \quad (2.2)$$

which is significantly larger than the 10^{-15} - 10^{-14} m range associated with the nuclear forces that cause scattering. Because of this, the incident wave function can be assumed to be composed entirely of s waves, meaning that the scattering is spherically symmetric. Assuming the neutron is scattering along the z -axis, the incident wavefunction can be written as

$$\psi_{\text{inc}} = \exp\{ikz\}, \quad (2.3)$$

where k is the magnitude of the scattering direction \mathbf{k} . Since scattering is assumed to be spherically symmetric, the scattered wavefunction is

$$\psi_{\text{sc}} = \frac{-b}{r} \exp\{ikr\}, \quad (2.4)$$

where b is a constant to be defined later. Using Eq. 2.3 and 2.4, the number of neutrons that impinging on the detector with surface area A subtended by $d\Omega$ (called dA) can be defined as

$$\Phi_{\text{sct}} = v dA |\psi_{\text{sc}}|^2 = v dA \frac{b^2}{r^2} = v b^2 \frac{dA}{r^2} = v b^2 d\Omega, \quad (2.5)$$

and the incident neutron flux can be written as

$$\Phi_{\text{inc}} = v|\psi_{\text{inc}}|^2 = v. \quad (2.6)$$

The differential cross section from Eq. 2.1 can be defined as the scattered flux over the incident flux:

$$\frac{d\sigma}{d\Omega} = \frac{v dA |\psi_{sc}|^2}{\Phi d\Omega} = \frac{v b^2 d\Omega}{v d\Omega} = b^2. \quad (2.7)$$

The variable b is known as the scattering length, and is complex. A large imaginary part indicates that the scattering interaction results in the formation of a compound nuclear resonance in the thermal or epithermal energy range, which results in large radiative capture relative to scattering. Since only few nuclides have large imaginary components near the energies of interest for thermal scattering, imaginary scattering lengths can be ignored for this analysis.

2.1.2 *Non-Static Target*

In practical situations, however, the target does not remain static, but rather changes when interacting with a neutron. Taking this into account, the differential cross section can be rewritten as

$$\left(\frac{d\sigma}{d\Omega}\right)_{(\lambda ks)_i \rightarrow (\lambda ks)_f} = \frac{1}{N\Phi\Delta\Omega} \sum_{k_f} W_{(\lambda ks)_i \rightarrow (\lambda ks)_f}, \quad (2.8)$$

where $W_{(\lambda ks)_i \rightarrow (\lambda ks)_f}$ (that supersedes C/η from Eq. 2.1), is the number of transitions per second with the scattering system in state λ_i , with initial momentum \mathbf{k}_i and initial spin s_i , to state λ_f with final momentum \mathbf{k}_f and final spin s_f . This transition rate can be evaluated using first-order perturbation to get what's known as Fermi's Golden Rule (a full derivation can be found in [13]):

$$W_{(\lambda ks)_i \rightarrow (\lambda ks)_f} = \frac{2\pi}{\hbar} |\langle \lambda_f \mathbf{k}_f s_f | V | \lambda_i \mathbf{k}_i s_i \rangle|^2 \rho_{\mathbf{k}_f s_f}(E_f), \quad (2.9)$$

where V is the interaction potential between the neutron and the target, and $\rho_{\mathbf{k}_f s_f}(E_f)$ is the density of the final neutron scattering state. This density can be defined as the number of momentum states in $d\Omega$ per unit energy interval. To evaluate this, the scattering experiment is assumed to be in a large cube with side length L , the wavefunctions can be described as a product of the spatial and spin functions. This leads to

$$\rho_{\mathbf{k}_f s_f}(E_f) dE_f = \frac{L^3}{8\pi^3} d\mathbf{k}_f = \frac{L^3}{8\pi^3} k_f^2 dk_f \Delta\Omega = \frac{L^3}{8\pi^3} \frac{mk_F}{\hbar^2} \Delta\Omega, \quad (2.10)$$

$$\rho_{\mathbf{k}_f s_f}(E_f) = \frac{L^3}{8\pi^3} \frac{mk_F}{\hbar^2} \Delta\Omega. \quad (2.11)$$

In the above equation, the last component is calculated from the relationship between kinetic energy and momentum. Mainly, $E_f = \hbar^2 k_f^2 / 2m$ and therefore $dE_f = \hbar^2 k_f dk_f / m$. The flux is then defined as number density times velocity, or $\varphi = v_i / L^3 = \hbar k_i / L^3 m$. Combining Eqs. 2.9 & 2.10 and substituting them into Eq. 2.8 yields

$$\left(\frac{d\sigma}{d\Omega}\right)_{(\lambda k s)_i \rightarrow (\lambda k s)_f} = \frac{1}{N} \frac{k_f}{k_i} \left(\frac{mL^3}{2\pi\hbar^2}\right)^2 |\langle \lambda_f \mathbf{k}_f s_f | V | \lambda_i \mathbf{k}_i s_i \rangle|^2. \quad (2.12)$$

To evaluate the bracketed function, the energies of the neutron and target need to be considered first. Using conservation of energy leads to

$$E = E_i - E_f = E_{\lambda_f} - E_{\lambda_i}, \quad (2.13)$$

where E will be used to define the energy transfer from the incident state to the final state. This leads to the first definition of the double differential scattering function,

$$\begin{aligned} \left(\frac{d\sigma}{d\Omega dE_f}\right)_{(\lambda k s)_i \rightarrow (\lambda k s)_f} \\ = \frac{1}{N} \frac{k_f}{k_i} \left(\frac{mL^3}{2\pi\hbar^2}\right)^2 |\langle \lambda_f \mathbf{k}_f s_f | V | \lambda_i \mathbf{k}_i s_i \rangle|^2 \delta(E - E_{\lambda_f} + E_{\lambda_i}). \end{aligned} \quad (2.14)$$

The scattering experiment does not measure the target state or the neutron spin. Because of this, the next step is to sum over all final target states λ_f and neutron spin states s_f , then average over all initial over all initial target states λ_i and neutron spin states s_i using probabilities of targets state P_{λ_i} and neutron spin states P_{s_i} . This is done below

$$\begin{aligned}
& \left(\frac{d\sigma}{d\Omega dE_f} \right)_{\mathbf{k}_i \rightarrow \mathbf{k}_f} \\
&= \frac{1}{N} \frac{k_f}{k_i} \left(\frac{mL^3}{2\pi\hbar^2} \right)^2 \sum_{\lambda_i S_i} P_{\lambda_i} P_{S_i} \sum_{\lambda_f S_f} |\langle \lambda_f \mathbf{k}_f S_f | V | \lambda_i \mathbf{k}_i S_i \rangle|^2 \\
& \times \delta(E - E_{\lambda_f} + E_{\lambda_i}).
\end{aligned} \tag{2.15}$$

Expanding the bracketed part of Eq. 2.15 is done using the definition of bra-ket notation (which can be found in [13]):

$$\langle \lambda_f \mathbf{k}_f S_f | V | \lambda_i \mathbf{k}_i S_i \rangle = \int \Psi_{\mathbf{k}_f S_f}^*(\mathbf{r}) \psi_{\lambda_f}^*(\mathbf{R}) V \Psi_{\mathbf{k}_i S_i}(\mathbf{r}) \psi_{\lambda_i}(\mathbf{R}) d\mathbf{R} d\mathbf{r}, \tag{2.16}$$

where $d\mathbf{R} = d\mathbf{R}_1 d\mathbf{R}_2 \dots d\mathbf{R}_n$, $d\mathbf{R}_j$ is a volume element for the j^{th} nucleus, $d\mathbf{r}$ is a volume element for the neutron, $\Psi_{\mathbf{k}_i S_i}(\mathbf{r})$ is the wavefunction of the incident neutron, $\psi_{\lambda_i}(\mathbf{R})$ is the wavefunction of the target before interacting with the neutron, $\Psi_{\mathbf{k}_f S_f}^*(\mathbf{r})$ is the complex conjugate of the wavefunction of the scattered neutron, and $\psi_{\lambda_f}^*(\mathbf{R})$ is the complex conjugate of the wavefunction of the target after interacting with the neutron.

Since there are many nuclei in the target, the potential term for the scattering system is rewritten as

$$V = \sum_j V_j(\mathbf{r} - \mathbf{R}_j) = \sum_j V_j(\mathbf{x}_j), \tag{2.17}$$

where $\mathbf{x}_j = \mathbf{r} - \mathbf{R}_j$. Additionally, since most scattering experiments use unpolarized beams, both neutron spin states are equiprobable for the incident and scattered neutron. If it is additionally assumed that the neutron again is a plane wave function along \mathbf{r} , then Eq. 2.16 is simplified down to

$$\begin{aligned} & \langle \lambda_f \mathbf{k}_f | V | \lambda_i \mathbf{k}_i \rangle \\ &= \sum_j \int e^{-i\mathbf{k}_f \cdot (\mathbf{x}_j + \mathbf{R}_j)} \psi_{\lambda_f}^*(\mathbf{R}_j) V_j(\mathbf{x}_j) e^{i\mathbf{k}_i \cdot (\mathbf{x}_j + \mathbf{R}_j)} \psi_{\lambda_i}(\mathbf{R}_j) d\mathbf{R} d\mathbf{r}. \end{aligned} \quad (2.18)$$

From here a few terms are defined to simplify the algebra. First, the difference in the scattering vectors is defined by the scattering vector \mathbf{q} as

$$\mathbf{q} = \mathbf{k}_i - \mathbf{k}_f. \quad (2.19)$$

This can also be thought of as the momentum transfer, since $\hbar\mathbf{k}$ is the momentum. Additionally, the following terms are defined

$$V_j(\mathbf{q}) = \int V_j(\mathbf{x}_j) e^{i\mathbf{q} \cdot \mathbf{x}_j} d\mathbf{x}_j, \quad (2.20)$$

$$\langle \lambda_f | e^{i\mathbf{q} \cdot \mathbf{R}_j} | \lambda_i \rangle = \int \psi_{\lambda_f}^* e^{i\mathbf{q} \cdot \mathbf{R}_j} \psi_{\lambda_i} d\mathbf{R}_j. \quad (2.21)$$

This is all done so that Eq. 2.18 can be rewritten as

$$\langle \lambda_f \mathbf{k}_f | V | \lambda_i \mathbf{k}_i \rangle = \sum_j V_j(\mathbf{q}) \langle \lambda_f | e^{i\mathbf{q} \cdot \mathbf{R}_j} | \lambda_i \rangle. \quad (2.22)$$

This relation cannot be further simplified until an expression for the potential is found. The Fermi Pseudopotential that reproduces the measured bound scattering length described in the next section is what will be used as this potential.

2.1.3 Fermi Pseudopotential

To further evaluate Eq. 2.22, suppose there is only 1 fixed nucleus as the target. This means that $j = 1$, and (after assuming the target nucleus is fixed at the origin so that $\mathbf{R}_1 = 0$ and $\lambda_f = \lambda_i$) that Eq. 2.18 can be rewritten as

$$\begin{aligned} \langle \lambda_f \mathbf{k}_f | V | \lambda_i \mathbf{k}_i \rangle &= \int \psi_{\lambda_f}^*(\mathbf{R}_1) \psi_{\lambda_i}(\mathbf{R}_1) d\mathbf{R}_1 \int V(\mathbf{r}) e^{i\mathbf{k}\cdot\mathbf{r}} d\mathbf{r} \\ &= \frac{1}{L^3} \int V(\mathbf{r}) e^{i\mathbf{k}\cdot\mathbf{r}} d\mathbf{r}, \end{aligned} \quad (2.23)$$

since the target wavefunction is normalized per unit volume, where the total volume equals L^3 . Then, since $k_f = k_i$, the above can be substituted into 2.12 to give

$$\left(\frac{d\sigma}{d\Omega} \right) = \left(\frac{m}{2\pi\hbar^2} \right)^2 \left| \int V(\mathbf{r}) e^{i\mathbf{q}\cdot\mathbf{r}} d\mathbf{r} \right|^2. \quad (2.24)$$

From here, an approximation of $V(\mathbf{r})$ is required. Since the potential range of the nuclear forces that cause neutron scattering are on the order of 10^{-15} m relative to interatomic distances on the order of 10^{-10} m, the potential can be approximated by a Dirac delta function,

$$V(\mathbf{r}) = a\delta(\mathbf{r}), \quad (2.25)$$

where a is a real constant. Substituting this into Eq. 2.24 gives

$$\left(\frac{d\sigma}{d\Omega}\right) = \left(\frac{m}{2\pi\hbar^2} \int a\delta(\mathbf{r})e^{iq\cdot\mathbf{r}} d\mathbf{r}\right)^2 = \left(\frac{ma}{2\pi\hbar^2}\right)^2 = b^2. \quad (2.26)$$

where the last equality follows from Eq. 2.7. Therefore,

$$a = \frac{2\pi\hbar^2}{m} b. \quad (2.27)$$

Using this, Eq. 2.25 becomes

$$V(\mathbf{r}) = \frac{2\pi\hbar^2}{m} b\delta(\mathbf{r}). \quad (2.28)$$

This is known as the Fermi Pseudopotential. It is worth noting here that this potential is not the actual potential of the nucleus. It was derived using Fermi's Golden Rule, which is similar to the Born approximation in that they are both first-order perturbation approximations. It is the potential that, when used with Fermi's Golden Rule (Eq. 2.9), gives the required result of isotropic scattering for a single fixed nucleus.

Reconsidering the target with many nuclei in the target, Eq. 2.28 can be generalized to multiple nuclei in the target,

$$V_j(\mathbf{x}_j) = \frac{2\pi\hbar^2}{m} b_j\delta(\mathbf{x}_j). \quad (2.29)$$

Inserting this result into Eq. 2.20 gives

$$V_j(\mathbf{q}) = \frac{2\pi\hbar^2}{m} b_j, \quad (2.30)$$

which means that, when combined with Eqs. 2.15 and 2.22

$$\frac{d^2\sigma}{d\Omega dE_f} = \frac{1}{N} \frac{k_f}{k_i} \sum_{\lambda_i} P_{\lambda_i} \sum_{\lambda_f} \left| \sum_j b_j \langle \lambda_f | e^{iq \cdot \mathbf{R}_j} | \lambda_i \rangle \right|^2 \delta(E - E_{\lambda_f} + E_{\lambda_i}). \quad (2.31)$$

From here, the Dirac delta function needs to be evaluated. To do this, it will be expanded in the time domain.

2.1.4 Time Domain

Before continuing, it is worthwhile to take a step back and review a bit of quantum mechanics that will be important later. Using the bra-ket notation introduced in Eq. 2.16,

$$\hat{H}|\lambda_i\rangle = E_{\lambda_i}|\lambda_i\rangle \quad \& \quad \hat{H}|\lambda_f\rangle = E_{\lambda_f}|\lambda_f\rangle, \quad (2.32)$$

where \hat{H} is the Hamiltonian of the scattering system. This Hamiltonian can be thought of as the sum of the kinetic and potential energy operators in quantum mechanics. This can be extended to show

$$e^{\frac{-i\hat{H}t}{\hbar}}|\lambda_i\rangle = e^{\frac{-iE_{\lambda_i}t}{\hbar}}|\lambda_i\rangle \quad \& \quad e^{\frac{-i\hat{H}t}{\hbar}}|\lambda_f\rangle = e^{\frac{-iE_{\lambda_f}t}{\hbar}}|\lambda_f\rangle, \quad (2.33)$$

by expanding the exponential function in a Taylor series. The closure relation [13] is also introduced here

$$\sum_{\lambda_f} \langle \lambda_i | \hat{A} | \lambda_f \rangle \langle \lambda_f | \hat{B} | \lambda_i \rangle = \langle \lambda_i | \hat{A} \hat{B} | \lambda_i \rangle. \quad (2.34)$$

With both of these relations, the derivation can continue. In order to take the energy component into consideration in Eq. 2.31, the Dirac Delta function is expanded using

$$\delta(E - E_{\lambda_f} + E_{\lambda_i}) = \frac{1}{2\pi\hbar} \int_{-\infty}^{\infty} e^{-\frac{it}{\hbar}(E - E_{\lambda_f} + E_{\lambda_i})} dt. \quad (2.35)$$

Additionally, the term in the brackets can be expanded

$$\begin{aligned} \left| \sum_{\lambda_f} \sum_j b_j \langle \lambda_f | e^{i\mathbf{q} \cdot \mathbf{R}_j} | \lambda_i \rangle \right|^2 &= \sum_{\lambda_f} \sum_{jj'} b_{j'}^* \langle \lambda_f | e^{i\mathbf{q} \cdot \mathbf{R}_j} | \lambda_i \rangle^* b_j \langle \lambda_f | e^{i\mathbf{q} \cdot \mathbf{R}_{j'}} | \lambda_i \rangle \\ &= \sum_{\lambda_f} \sum_{jj'} b_{j'} b_j \langle \lambda_i | e^{-i\mathbf{q} \cdot \mathbf{R}_j} | \lambda_f \rangle \langle \lambda_f | e^{i\mathbf{q} \cdot \mathbf{R}_{j'}} | \lambda_i \rangle. \end{aligned} \quad (2.36)$$

The latter is because the scattering length is assumed to be real. Inserting this relation (along with Eq. 2.35) into Eq. 2.31 gives

$$\begin{aligned} \frac{d^2\sigma}{d\Omega dE_f} &= \frac{1}{N} \frac{k_f}{k_i} \frac{1}{2\pi\hbar} \sum_{\lambda_i} P_{\lambda_i} \sum_{\lambda_f} \sum_{jj'} b_{j'} b_j \\ &\times \int_{-\infty}^{\infty} \langle \lambda_i | e^{-i\mathbf{q} \cdot \mathbf{R}_j} | \lambda_f \rangle \langle \lambda_f | e^{i\mathbf{q} \cdot \mathbf{R}_{j'}} | \lambda_i \rangle e^{-\frac{it}{\hbar}(E - E_{\lambda_f} + E_{\lambda_i})} dt. \end{aligned} \quad (2.37)$$

From here, the bra-ket notation relation from Eq. 2.33 is applied to give

$$\begin{aligned} \frac{d^2\sigma}{d\Omega dE_f} &= \frac{1}{N} \frac{k_f}{k_i} \frac{1}{2\pi\hbar} \sum_{\lambda_i} P_{\lambda_i} \sum_{\lambda_f} \sum_{jj'} b_{j'} b_j \\ &\times \int_{-\infty}^{\infty} \langle \lambda_i | e^{-iq \cdot \mathbf{R}_j} | \lambda_f \rangle \left\langle \lambda_f \left| e^{\frac{i\hat{H}t}{\hbar}} e^{iq \cdot \mathbf{R}_{j'}} e^{-\frac{i\hat{H}t}{\hbar}} \right| \lambda_i \right\rangle e^{-\frac{itE}{\hbar}} dt. \end{aligned} \quad (2.38)$$

Before the final equations are derived, a few more definitions and conventions are required. First, the initial probability of states in the target, P_{λ_i} , is assumed to be given by a Boltzmann distribution:

$$P_{\lambda_i} = \frac{e^{-\frac{E_{\lambda_i}}{k_B T}}}{\sum_{\lambda_i} e^{-\frac{E_{\lambda_i}}{k_B T}}}. \quad (2.39)$$

Then the Heisenberg operator is defined for convenience:

$$\hat{\mathbf{R}}_j(t) = e^{\frac{i\hat{H}t}{\hbar}} e^{iq \cdot \mathbf{R}_j} e^{-\frac{i\hat{H}t}{\hbar}}. \quad (2.40)$$

It's worth noting that $\mathbf{R}_j(0) = \mathbf{R}_j$. Finally, the thermal operator is defined as

$$\langle A \rangle = \sum_{\lambda_i} P_{\lambda_i} \langle \lambda_i | \hat{A} | \lambda_i \rangle. \quad (2.41)$$

Combining these conventions into Eq. 2.38 gives

$$\frac{d^2\sigma}{d\Omega dE_f} = \frac{1}{N} \frac{k_f}{k_i} \frac{1}{2\pi\hbar} \sum_{jj'} b_{j'} b_j \int_{-\infty}^{\infty} \langle e^{-iq \cdot \hat{\mathbf{R}}_j(0)} e^{iq \cdot \hat{\mathbf{R}}_{j'}(t)} \rangle e^{-\frac{itE}{\hbar}} dt. \quad (2.42)$$

The last step involves dealing with the scattering lengths, $b_{j'}$ & b_j . It is impossible to know the exact scattering length of each individual nuclide in the target due to the random distribution of spins for each isotope and of isotopes in a target. Because of this, it is easiest to simply take an average over all spin states and isotopes in target

$$\frac{d^2\sigma}{d\Omega dE_f} = \frac{1}{N} \frac{k_f}{k_i} \frac{1}{2\pi\hbar} \sum_{jj'} \overline{b_{j'} b_j} \int_{-\infty}^{\infty} \langle e^{-i\mathbf{q}\cdot\hat{\mathbf{R}}_j(0)} e^{i\mathbf{q}\cdot\hat{\mathbf{R}}_{j'}(t)} \rangle e^{\frac{-itE}{\hbar}} dt. \quad (2.43)$$

2.1.5 Coherent and Incoherent Scattering

While Eq. 2.43 sufficiently describes the double differential scattering cross section, it is worthwhile to break it down into terms that are easier to grasp. The first step is therefore to define the dynamic structure factor (DSF) of nuclide j and j' as

$$S_{jj'}(\mathbf{q}, E) = \frac{1}{2\pi\hbar} \int_{-\infty}^{\infty} \frac{1}{N} \langle e^{-i\mathbf{q}\cdot\hat{\mathbf{R}}_j(0)} e^{i\mathbf{q}\cdot\hat{\mathbf{R}}_{j'}(t)} \rangle e^{\frac{-itE}{\hbar}} dt. \quad (2.44)$$

This DSF has often times been calculated as $S_{jj'}(\mathbf{q}, \omega)$, where ω is the frequency given by $\omega = E/h$, where h is Planck's Constant. This work will deal with the energy E to avoid confusion between the two. Next, the spin states are assumed to be uncorrelated from each other, meaning that

$$\overline{b_{j'} b_j} = \begin{cases} \overline{b^2} & j \neq j' \\ \overline{b^2} & j = j' \end{cases} \quad (2.45)$$

When Eqs. 2.44 and 2.45 are inserted into Eq. 2.43, the resulting equation is

$$\frac{d^2\sigma}{d\Omega dE_f} = \frac{k_f}{k_i} \left[\bar{b}^2 \sum_{\substack{jj' \\ j \neq j'}} S_{jj'}(\mathbf{q}, E) + \bar{b}^2 \sum_j S_{jj}(\mathbf{q}, E) \right], \quad (2.46)$$

which can be rewritten as

$$\frac{d^2\sigma}{d\Omega dE_f} = \frac{k_f}{k_i} \left[\bar{b}^2 \sum_{jj'} S_{jj'}(\mathbf{q}, E) + (\bar{b}^2 - \bar{b}^2) \sum_j S_{jj}(\mathbf{q}, E) \right]. \quad (2.47)$$

The first term of above equation is known as the coherent cross section, and the second term is known as the incoherent cross section. The coherent cross section can be thought of as the correlation between positions of pairs of nuclei at different times. This gives rise to interference effects, and is strongly dependent on the relative arrangement of atoms in a structure. It is this reason why coherent scattering is much more important in crystalline solids, such as graphite or polyethylene. On the contrary, the incoherent cross section depends on the correlations at different times; it does not give interference effects.

To further condense everything down, the following terms are defined

$$\sigma_{\text{coh}} = 4\pi\bar{b}^2 \quad \sigma_{\text{inc}} = 4\pi(\bar{b}^2 - \bar{b}^2) \quad \sigma_{\text{b}} = \sigma_{\text{coh}} + \sigma_{\text{inc}}, \quad (2.48)$$

$$S_{\text{coh}}(\mathbf{q}, E) = \sum_{jj'} S_{jj'}(\mathbf{q}, E) \quad S_{\text{inc}}(\mathbf{q}, E) = \sum_j S_{jj}(\mathbf{q}, E). \quad (2.49)$$

Using these, Eq. 2.47 can be written as

$$\frac{d^2\sigma}{d\Omega dE_f} = \frac{k_f}{k_i} \left[\frac{\sigma_{\text{coh}}}{4\pi} S_{\text{coh}}(\mathbf{q}, E) + \frac{\sigma_{\text{inc}}}{4\pi} S_{\text{inc}}(\mathbf{q}, E) \right]. \quad (2.50)$$

Condensing further, the total dynamics structure factor is defined as

$$S(\mathbf{q}, E) = \frac{\sigma_{\text{coh}}}{\sigma_b} S_{\text{coh}}(\mathbf{q}, E) + \frac{\sigma_{\text{inc}}}{\sigma_b} S_{\text{inc}}(\mathbf{q}, E), \quad (2.51)$$

which leads to

$$\frac{d^2\sigma}{d\Omega dE_f} = \frac{k_f \sigma_b}{k_i 4\pi} S(\mathbf{q}, E). \quad (2.52)$$

In the field of nuclear engineering, the so-called ‘‘scattering law’’, $S(\alpha, \beta)$, is defined by the unit-less variables α , which correlates to momentum transfer, and β , which correlates to energy transfer. The scattering law, as well as the unit-less variables α and β are defined as

$$S(\alpha, \beta) = k_b T e^{\frac{E}{2k_B T}} S(\mathbf{q}, E), \quad (2.53)$$

$$\alpha = \frac{q^2 \hbar^2}{2M k_B T} = \frac{E_i + E_f - 2\mu \sqrt{E_i E_f}}{A k_B T}, \quad (2.54)$$

$$\beta = \frac{-E}{k_B T} = \frac{E_f - E_i}{k_B T}. \quad (2.55)$$

This leads to

$$\frac{d^2\sigma}{d\Omega dE_f} = \frac{\sigma_b}{4\pi k_b T} \sqrt{\frac{E_f}{E_i}} e^{-\frac{\beta}{2}} S(\alpha, \beta). \quad (2.56)$$

From here, there is still one problem that has not been addressed: how to solve the thermal averaging and deal with the Heisenberg operators in Eq.2.44. There are two ways to go about it described below: using the Van Hove Theory and the Gaussian approximation.

2.1.6 Van Hove Theory

The crux of the Van Hove Theory is that scattering can be determined by scattering functions [14]. Specifically, the positions of the particles at a specific time are correlated to the momentum and energy transfer. To explain, the DSF introduced in Eq. 2.44 can be defined by

$$S(\mathbf{q}, E) = \frac{1}{2\pi\hbar} \int F(\mathbf{q}, t) e^{\frac{-iEt}{\hbar}} dt, \quad (2.57)$$

where $F(\mathbf{q}, t)$ is the intermediate structure factor. From here, the intermediate structure factor is defined as

$$F(\mathbf{q}, t) = \int G(\mathbf{r}, t) e^{i\mathbf{q}\cdot\mathbf{r}} d\mathbf{r}, \quad (2.58)$$

where $G(\mathbf{r}, t)$ is the space-time correlation function. The above equations can be thought of in the following way: space-time correlation function is a function dependent on the position of the neutrons relative to the target at a time t . The intermediate structure factor

is the Fourier transform in momentum space of the space-time correlation function. The DSF, in turn, is the Fourier transform in energy space of the intermediate structure factor.

The space-time correlation function is defined as

$$G(\mathbf{r}, t) = \frac{1}{N} \left\langle \sum_{jj'} \int \delta(\mathbf{r} + \hat{\mathbf{R}}_j(0) - \mathbf{r}') \delta(\mathbf{r}' - \hat{\mathbf{R}}_{j'}(t)) d\mathbf{r}' \right\rangle, \quad (2.59)$$

where the Heisenberg operators introduced in Eq. 2.40 are used. This form is not very useful from a computational standpoint for a few reasons. The Heisenberg operators are still present which, in addition to being difficult to solve for analytically, do not commute, meaning the integral cannot be performed. If their lack of commutation is ignored, the integral can be carried out to obtain the so-called ‘classical’ form of the space-time correlation function

$$G^{cl}(\mathbf{r}, t) = \frac{1}{N} \left\langle \sum_{jj'} \delta(\mathbf{r}' - \hat{\mathbf{R}}_{j'}(t) + \hat{\mathbf{R}}_j(0)) \right\rangle. \quad (2.60)$$

From this, the classical intermediate structure factor can be defined as

$$F^{cl}(\mathbf{q}, t) = \int G^{cl}(\mathbf{r}, t) e^{i\mathbf{q}\cdot\mathbf{r}} d\mathbf{r} = \frac{1}{N} \langle e^{-i\mathbf{q}\cdot\hat{\mathbf{R}}_j(0)} e^{i\mathbf{q}\cdot\hat{\mathbf{R}}_{j'}(t)} \rangle. \quad (2.61)$$

This form is still problematic as the Heisenberg operator and thermal averaging operator are both still present. To deal with this, the Heisenberg operators are replaced by the classical position of the particles and the thermal averaging is replaced by classical

ensemble averages. Making these substitutions comes at the price losing the universal detailed balance relation

$$S(\mathbf{q}, E) = S(-\mathbf{q}, -E)e^{-\frac{E}{kT}}, \quad (2.62)$$

as well as a loss of the relation of odd moments

$$\langle E^{2n+1} \rangle = \int_{-\infty}^{\infty} dE E^{2n+1} S(\mathbf{q}, E). \quad (2.63)$$

To deal with this approximation, several different semi-classical approximations have been developed to improve the accuracy of the DSF ([15] [16] [17]). Using these semi-classical approximations improves the relation from Eq. 2.63 to be accurate in the first moment, but the higher odd moments are still inaccurate [18].

2.1.7 Gaussian Approximation

An alternative to the Van Hove theory is to calculate the DSF directly using the Gaussian approximation. This approximation only applies to the incoherent component of the double differential scattering cross section, and is sometimes referred to as the ‘‘Incoherent approximation’’. In this scenario, the space-time correlation function is defined as

$$G(\mathbf{r}, t) = (2\pi\Gamma(t))^{-\frac{3}{2}} e^{-\frac{r^2}{2\Gamma(t)}}, \quad (2.64)$$

where $\Gamma(t)$ is the width function, which is interpreted as the mean square departure of the particle from the origin after time t . The associated intermediate structure factor is therefore

$$F(\mathbf{q}, t) = \int G(\mathbf{r}, t) e^{i\mathbf{q}\cdot\mathbf{r}} d\mathbf{r} = \exp\left[-\frac{q^2\Gamma(t)}{2}\right]. \quad (2.65)$$

The width function can be thought of as the mean square departure of a particle at time t from its location at $t=0$. There are multiple ways to calculate this width function [19]. In this framework, the width function will be calculated using the frequency distribution (also known as the density of states) as shown below

$$\Gamma(t) = \frac{\hbar}{M} \int_0^{\infty} d\omega \frac{g(\omega)}{\omega} \left\{ \coth\left(\frac{\hbar\omega}{2k_B T}\right) (1 - \cos(\omega t)) - i \sin(\omega t) \right\}, \quad (2.66)$$

where $g(\omega)$ is the frequency distribution. This particular width function is valid for an arbitrary target, regardless of whether it's a solid or liquid.

This process of obtaining the incoherent scattering law is what is used by NJOY [8]. It can be shown that the subsequent DSF satisfies the universal detailed balance relation mentioned in Eq. 2.62, as well as the first odd moment in Eq. 2.63.

2.2 Unified Monte Carlo

Nuclear data at energy ranges above the thermal neutron energy group has traditionally been evaluated using the generalized least squares (GLS) method. This method is based on the principle of maximum entropy and is applicable to many

situations, but does have the drawback of requiring sensitivities that would require modifications to the molecular dynamics code [20]. Because of this limitation, a newer, less restrictive model was deemed necessary for evaluating thermal scattering data. The Unified Monte Carlo (UMC) method was first described by Smith [21] and follows from Bayes Theorem and the Principle of Maximum Entropy [22]. In the following description, an experiment containing n experimental data points is represented by \mathbf{y}_E , it's associated covariance matrix is \mathbf{V}_E , simulation results (calculated using a nuclear model, or some computer code) containing m data points is represented by \mathbf{x}_C , and it's associated covariance matrix is \mathbf{V}_C . Bayes Theorem gives the posterior probability density function (PDF) $p(\mathbf{x})$ in the following form

$$p(\mathbf{x}) = \mathcal{N}L(\mathbf{y}_E, \mathbf{V}_E|\mathbf{x})p_o(\mathbf{x}|\mathbf{x}_C\mathbf{V}_C), \quad (2.67)$$

where \mathcal{N} is a normalization constant, $L(\mathbf{y}_E, \mathbf{V}_E|\mathbf{x})$ is a likelihood PDF (dependent on experimental data), and $p_o(\mathbf{x}|\mathbf{x}_C\mathbf{V}_C)$ is the prior PDF (dependent on the simulation data), and \mathbf{x} is a collection of m random variables. The normalization constant is chosen so that the posterior PDF integrates to unity when integrated over the entire domain space. Using this notation, the mean value of each random variable x_i in the collection of random variables \mathbf{x} and the elements of its covariance matrix are defined as

$$\langle x_i \rangle = \int x_i p(\mathbf{x}) d\mathbf{x}, \quad (2.68)$$

$$(\mathbf{V})_{i,j} = \langle x_i x_j \rangle - \langle x_i \rangle \langle x_j \rangle. \quad (2.69)$$

There are currently two different UMC methodologies that are used: UMC-G and UMC-B.

2.2.1 UMC-G

The Principle of Maximum Entropy states that, if a collection of random variables is summarized by only their mean values and covariance matrix, the optimal choice for the PDF is a multivariate Gaussian function. This leads to the following likelihood function

$$L(\mathbf{y}_E, \mathbf{V}_E | \mathbf{x}) \sim \exp \left\{ -\frac{(\mathbf{y} - \mathbf{y}_E)^T \cdot \mathbf{V}_E^{-1} \cdot (\mathbf{y} - \mathbf{y}_E)}{2} \right\}, \quad (2.70)$$

and the following prior function

$$p_o(\mathbf{x} | \mathbf{x}_C, \mathbf{V}_C) \sim \exp \left\{ -\frac{(\mathbf{x} - \mathbf{x}_C)^T \cdot \mathbf{V}_C^{-1} \cdot (\mathbf{x} - \mathbf{x}_C)}{2} \right\}. \quad (2.71)$$

Here, \mathbf{y}_E , stands for experimental data, in our case it would be the measured double differential cross section and \mathbf{x}_C would be the mean value of some number of computer simulation runs which calculate the DSF $S(\mathbf{q}, E)$. The variable \mathbf{y} is therefore defined as $\mathbf{y} = f(\mathbf{x})$, where f contains n scalar functions, each of whose variables are one or more of the elements of random variable \mathbf{x} . Specifically, f would be a process to transform the random variable \mathbf{x} associated with the DSF, to the double differential cross section of incident energy E_i , final energy E_f , and scattering angle θ .

Using these definitions for prior and likelihood functions, the integrals in Eqs. 2.68 and 2.69 become

$$\langle x_i \rangle = \lim_{K \rightarrow \infty} \frac{\sum_{k=1}^K x_{ik} p(\mathbf{x}_k)}{\sum_{k=1}^K p(\mathbf{x}_k)}, \quad (2.72)$$

$$\langle \mathbf{V} \rangle_{i,j} = \lim_{K \rightarrow \infty} \frac{\sum_{k=1}^K x_{ik} x_{jk} p(\mathbf{x}_k)}{\sum_{k=1}^K p(\mathbf{x}_k)} - \langle x_i \rangle \langle x_j \rangle, \quad (2.73)$$

where K represents the number of Monte Carlo histories tallied. From here, the random variable is sampled using a Monte Carlo sampling scheme. The two most common sampling methods are the brute force method and the Metropolis algorithm. It has been shown, however, that Metropolis algorithm will converge on an answer several orders of magnitude quicker than a brute force method would [21].

The UMC-G method has the benefit of creating an analytic approximation for the posterior that can be readily sampled. One of its main shortcomings is the need for the simulation covariance matrix. It also has issues with higher-order distribution moments, leading to biases in cases where non-linear effects and distribution skewness and kurtosis are present.

2.2.2 UMC-B

An alternate to the UMC-G method is the UMC-B method [23]. This method came about from the realization that certain analyses excessively rely on nuclear modelling and inadequately consider experimental data. The UMC-B formulation, like UMC-G, is founded on the ideals of Bayes Theorem and the Principle of Maximum Entropy. Unlike in UMC-G, however, the mean values of the simulation data \mathbf{x}_C and its associated

covariance matrix \mathbf{V}_C are not calculated. Instead, a collection of scalar weighting values ω_k are calculated for each simulation k . These weighting values are given by

$$\omega_k = \exp\left\{-\frac{1}{2}[(\mathbf{y}_k - \mathbf{y}_E)^T \cdot \mathbf{V}_E^{-1} \cdot (\mathbf{y}_k - \mathbf{y}_E)]\right\}. \quad (2.74)$$

As in the UMC-G case, $\mathbf{y}_k = f(\mathbf{x}_{Ck})$, where \mathbf{x}_{Ck} is calculated using model parameters sampled using the same prior distribution as in UMC-G. This weighting value can be thought of as a measure of the deviation between the experimental data \mathbf{y}_E from the simulation data \mathbf{y}_k for the k^{th} simulation history. Once the simulation values are calculated, the mean values and covariance matrix can be calculated using

$$\langle x_i \rangle = \lim_{K \rightarrow \infty} \frac{\sum_{k=1}^K x_{ik} \omega_k}{\sum_{k=1}^K \omega_k}, \quad (2.75)$$

$$\langle \mathbf{V} \rangle_{i,j} = \lim_{K \rightarrow \infty} \frac{\sum_{k=1}^K x_{ik} x_{jk} \omega_k}{\sum_{k=1}^K \omega_k} - \langle x_i \rangle \langle x_j \rangle. \quad (2.76)$$

A benefit to the UMC-B method, aside from not needing to calculate the simulation covariance matrix, is that all information in the prior function is preserved, including the non-linear terms neglected by the UMC-G case. A drawback, however, is that the sampling range for the nuclear model parameters must be sufficiently large to ensure that there are no biases. This means that there will be model parameters sampled that can lead to un-physical results and must be rejected, which wastes computational resources.

2.3 Water Models

As mentioned in the introduction, water is very difficult to model. Here the empirically-based models of water models will be discussed. These models, rather than the more accurate polarization or *ab initio* methods, are used because they will be used in a classical molecular dynamics (MD) code system that cannot handle *ab initio* models. In general, the empirical models of water are categorized based on the number of ‘sites’ for the model. Each site represents an interaction point with which another site may have an interaction with, either nuclear or electromagnetic. The number of interaction sites can range from 3 to 6, depending on the model used. An example configuration of a 4-site model is shown below in Figure 3.

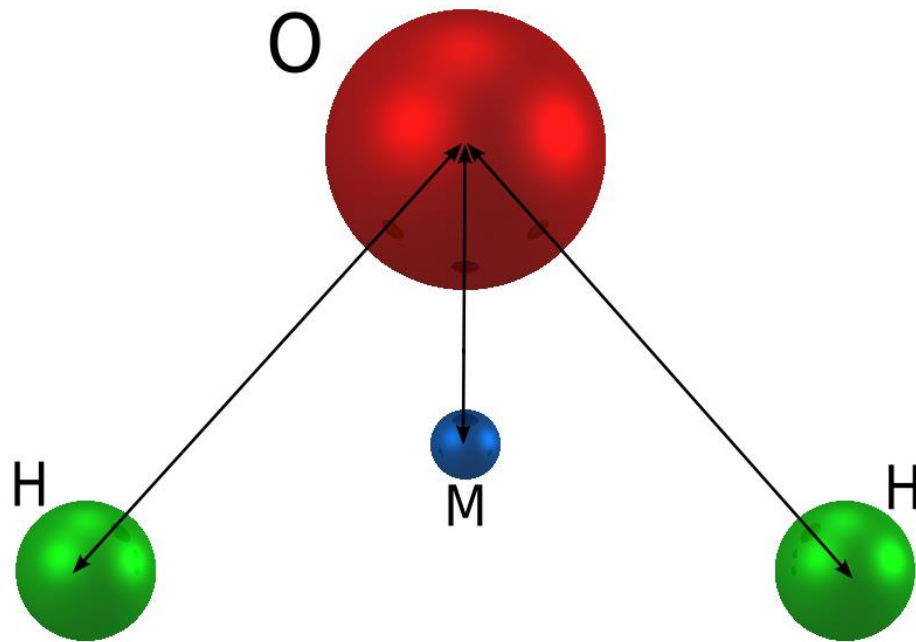


Figure 3. 4-Site Water Molecule

In general, each of the models is characterized by a potential that can contain 2 separate components: non-bonded and bonded terms. The non-bonded terms used in water are the Coulomb potential and the Lennard-Jones (LJ) potential. The Coulomb potential describes how charged particles interact with each other using the electromagnetic force and has the functional form

$$V_C(r_{ij}) = \frac{1}{4\pi\epsilon_o} \frac{q_i q_j}{\epsilon_r r_{ij}}, \quad (2.77)$$

where ϵ_o is the permittivity of free space, ϵ_r is the dielectric constant, q_i and q_j are the charges of particles i and j , and r_{ij} is the distance between particles i and j . Because there is no limit to the range of this potential, most MD codes will cutoff interactions longer than a given length. Long range electrostatics are handled using particle-mesh Ewald method [24].

The Lennard-Jones potential describes how neutrally-charged particles and molecules interact with each other. This term has the function form of

$$V_{LJ}(r_{ij}) = 4\epsilon \left(\left(\frac{\sigma_{ij}}{r_{ij}} \right)^{12} - \left(\frac{\sigma_{ij}}{r_{ij}} \right)^6 \right), \quad (2.78)$$

where ϵ is the depth of the potential well, σ_{ij} is the finite distance between particles i & j at which the potential changes from repulsive to attractive, as seen in Figure 4. The potential has a repulsive effect (corresponding to a positive value) for small distances $r < \sigma$, and then an attractive effect (corresponding to a negative value) for distances $r > \sigma$ while asymptotically approaching zero. Like the Coulomb potential, there is no

maximum range for the Lennard-Jones potential, so computer codes use approximations for when to stop calculating its contributions to the potential of a particle.

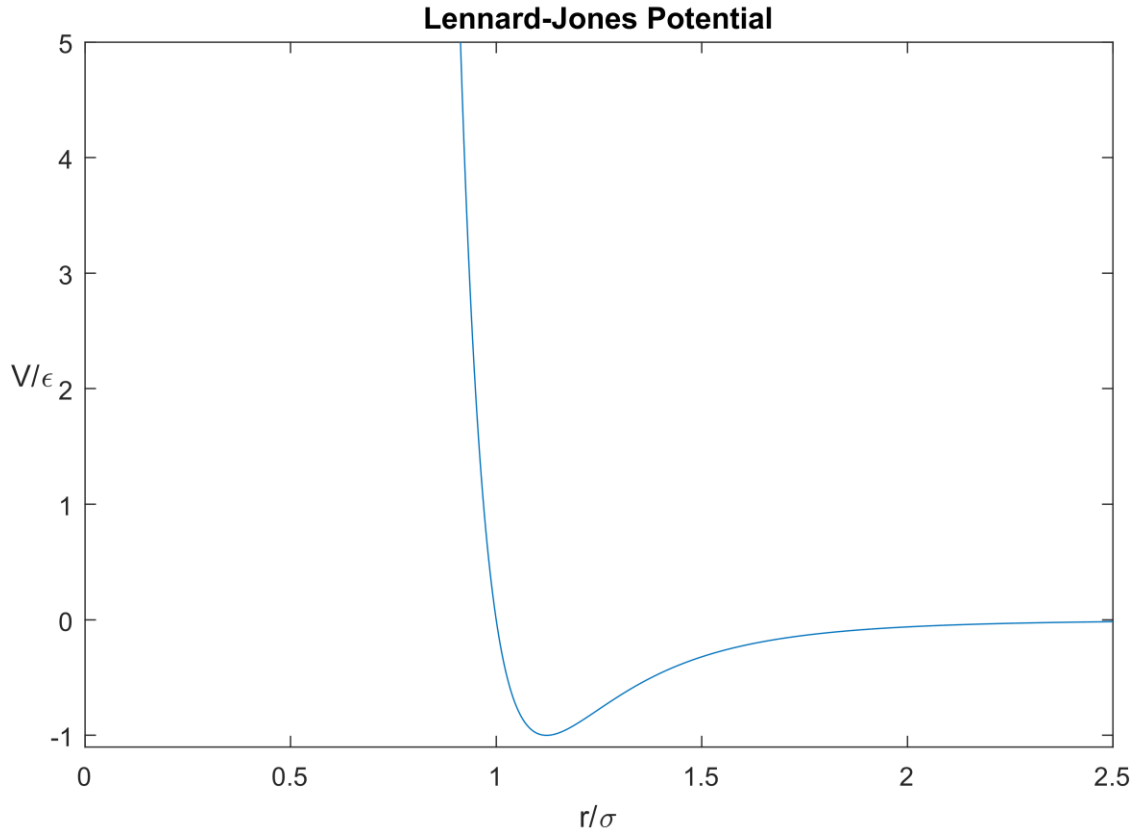


Figure 4. Lennard-Jones Potential

Bonded terms, on the other hand, deal with the interactions within an atom. In water, there are 2 dominant bonded interactions that are used: bond stretching and bond angle. The most common bond stretching form that is commonly used in water is the harmonic potential, which has the form

$$V_{bH}(r_{ij}) = \frac{1}{2}k_{ij}^b(r_{ij} - b_{ij,o})^2, \quad (2.79)$$

where k_{ij}^b is the bond strength between particles i and j , and $b_{ij,o}$ is the equilibrium length between particles i and j . There are a few potentials, however, where anharmonic bond stretching is required. For these cases, the Morse potential is used:

$$V_{bM}(r_{ij}) = D_{ij} \left[1 - e^{-\beta_{ij}(r_{ij}-b_{ij,o})} \right]^2, \quad (2.80)$$

where D_{ij} is the depth of the potential well and β_{ij} defines the steepness of the well. A plot comparing the two bond potentials is shown below in Figure 5. It can be seen that, for increasing radius, the Morse potential does exhibit slightly anharmonic behavior.

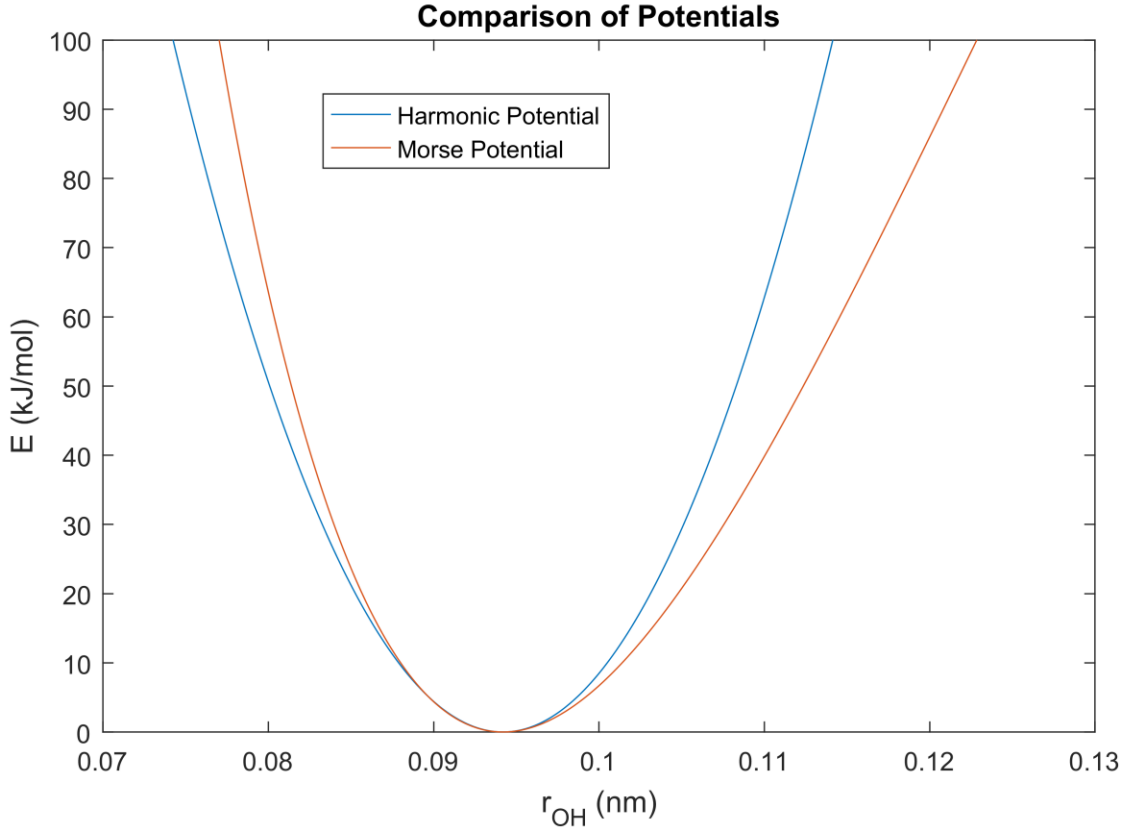


Figure 5. Comparison of bond potentials

The other angle bond term refers to how the molecular vibrations affect the angle of the molecule. In the case of water, it refers to the only angle in the molecule: the H-O-H angle, which is represented as a harmonic function (similar to Eq. 2.79)

$$V_a(\theta_{ijk}) = \frac{1}{2} k_{ijk}^{\theta} (\theta_{ijk} - \theta_{ijk}^0)^2, \quad (2.81)$$

where k_{ijk}^{θ} is the bond strength, θ_{ijk} is the angle between the three atoms, and θ_{ijk}^0 is the equilibrium angle between the three atoms.

CHAPTER 3. FRAMEWORK OVERVIEW & RESULTS

Here, the specific details of the framework are presented and discussed. The light water experimental dataset used to validate the framework is first described. The process for generating thermal scattering kernels is detailed, and the double differential cross sections resulting from the framework are then validated against other experimental data not used in the original UMC fitting procedure.

3.1 Experimental Data

The experimental data was gathered from the Fine-Resolution Fermi Chopper Spectrometer (SEQUOIA) detector at the ORNL Spallation Neutron Source (SNS) in 2005 by a research group from Rensselaer Polytechnic Institute (RPI). The data was collected at incident energies of 55, 160, 250, 600, 1000, 3000, and 5000 meV between scattering angles of 3° - 58° with 1° increments. The energy resolution for the double differential cross sections are 0.5 meV for the 55 meV case, 1 meV for the 160 meV case, and 2 meV for the remaining 5 cases. Each experiment was carried out at a temperature of 300 K.

The SEQUOIA detector is a time-of-flight spectrometer, which works by limiting the incident neutron energy to one specific energy using metal cylinders called choppers. These choppers have a wedge holed out of them that, when rotating at a specific speed, allows only energy of neutron through. These neutrons then hit the sample, which is a 0.1mm thick sample of light water in an aluminum can. The sample was chosen to be thin

to reduce the effects of multiple scattering. The scattered neutrons then travel to one of the detectors, which tally the time when the neutrons arrived, meaning that the scattered energy can be calculated. Two separate experimental runs were performed and averaged to improve the accuracy of the results. A third run where the water is removed is then done to get the effects of the aluminum can, so that it can be subtracted off the previous two runs.

3.2 Framework

To generate the mean DSF, the UMC method will be used to compare against the experimental DDCS described above. The decision to use DDCS was based on the fact that it is an experimentally measurable quantity, while the DSF cannot be experimentally measured. There is no reason why total cross section could not be used instead, but the DDCS measurements should give a better understanding into the totality of the DSF, while the total cross section would give an understanding to its integral properties, which may hide some underlying that would be found by comparing to the DDCS.

The first step of the framework is to obtain the trajectory data for water. For this, the code GROMACS [25] was used due to its highly customizable input parameters. In addition, the ability to create new parameter files means that any feasible model for water can be used. For this case, the TIP4P/2005f potential [26] will be used. This was chosen because the potential was originally fitted to yield a more accurate frequency distribution (also known as a density of states or phonon density) for water. Because of this, the potential equation (a combination of Eqs. 2.77, 2.78, 2.80 and 2.81) has the form of

$$\begin{aligned}
V = & \sum_{ij} K_b \left(1 - e^{\beta_{ij}(r_{ij}-b_{ij,o})}\right)^2 + \sum_{ijk} K_{ijk,\theta} (\theta_{ijk} - \theta_{ijk,o})^2 \\
& - \sum_{ij} \frac{q_i q_j}{\epsilon_r r_{ij}} + \sum_{ij} 4\epsilon_{ij} \left(\left(\frac{\sigma_{ij}}{r_{ij}}\right)^{12} - \left(\frac{\sigma_{ij}}{r_{ij}}\right)^6 \right). \tag{3.1}
\end{aligned}$$

From this equation, a total of eight parameters will be perturbed based on a Gaussian distribution: K_b , b_o , β , K_θ , θ_o , ϵ , and σ . Not shown in the above equation is the parameter that dictates the distance the dummy particle is from the oxygen atom, d_o , which will also be modified. The published values of these variables are shown below in Table 1.

Table 1. Published TIP4P/2005f parameters

Parameter (units)	Value
D_r (kJ/mol)	4.3258E+02
β (1/nm)	2.2870E+01
b_o (nm)	9.4190E-02
K_θ (kJ/(mol radian ²))	3.6781E+02
θ_o (degrees)	1.0740E+02
ϵ (kJ/mol)	7.7490E-01
σ (nm)	3.1644E-02
d_o (nm)	1.5460E-03

The molecular dynamics simulation is broken up into 4 steps, as outlined in [27]. First, a system of 512 water molecules in a cube with sides of 2.407 nm is minimized using the steepest descent method over 500,000 steps, where the positions of the atoms are changed such that the total force in the system is reduced to a minimum. Then, the

system is simulated for 100 ps with a 0.1 fs time step in an NVT ensemble (where the number of molecules, volume, and temperature are held constant). The temperature is coupled using a Nose-Hoover extended ensemble. Next, an NPT simulation (where the number of molecules, pressure, and temperature are held constant) is carried out for 1 ns with a 0.1 fs time step. Again, the temperature is coupled using a Nose-Hoover extended ensemble, and the pressure is coupled using the Parrinello-Rahnam scheme, where the pressure coupling of the box vectors are subject to the equations of motion. Finally, an NVE ensemble (where the number of molecules, pressure, and total energy are held constant) is performed for 100 ps with a 0.1 fs time step. In this step, the MD frames are saved every 0.4 fs. In these runs, a cutoff length of 0.8 nm is used for the electrostatic and Lennard-Jones potentials, and periodic boundary conditions are assumed (so that particles leaving the system in the +x direction are simulated as entering in the system from the -x direction, for example).

Once the MD trajectories are saved, the next step is to use these trajectories to calculate the DSF. For this application of the framework, the Gaussian approximation (described in Section 2.1.7) is used. This approximation is valid for light water because the incoherent scattering cross section for light water (160.54 b) is much greater than the coherent cross section (7.7486 b). To calculate the DSF using the Gaussian approximation, the density of state is required. This is calculated using the velocity autocorrelation as shown in Eq. 3.2

$$g(\omega) = \int_0^{\infty} dt \cos(\omega t) \text{vacf}(t), \quad (3.2)$$

where $\text{vacf}(t)$ is the velocity autocorrelation function defined as

$$\text{vacf}(t) = \langle \mathbf{v}(0)\mathbf{v}(t) \rangle_c, \quad (3.3)$$

where $\langle \rangle_c$ is the classical averaging operator. The velocity autocorrelation function is calculated by GROMACS. Traditionally when calculating the thermal scattering law, this density of states is used as an input for NJOY, which performs all of the necessary calculations. However, since the purpose of this framework is to create a generalized framework, NJOY will only be used to prepare the cross sections for validation in MCNP, and is not necessary for the calculation of the thermal scattering law.

Using this density of state, the width function from Eq. 2.66 is broken up into two steps: short time scales and long time scales. This was done to better capture the effects of the intermediate structure factor at both time scales without the need for one large finely-spaced time scale. Then the intermediate structure factor is calculated using a logarithmically spaced q vector again to capture the effects of very small momentum transfer and very large momentum transfer. The Fourier transfer is then used to calculate the DSF.

To better compare these simulated results against the experimental data, a simplified model of the SNS detector was modeled in MCNP, where a monoenergetic beam of neutrons was fired at a cube of water, and the scattering results were tallied at rings meant to represent how the SEQUOIA detector tallied the scattering events. Since MCNP is being used, the DSF is converted to ACE format using NJOY [8]. The SEQUOIA detector resolution was applied afterwards. Finally, the UMC procedure is done. In this

framework, the UMC-B method will be used, as it has the benefit of not requiring the calculation of the covariance matrix of the simulation data.

Before the framework was fully implemented, a small set of ensembles were run where the TIP4P/2005f parameters were not perturbed. Instead, only the initial position of the atoms in the simulation was changed. This was done to see how the weighting function might change between ensembles where the only difference should be statistical noise and the random movements of the molecules. This run yielded a surprising conclusion; the overall variation of the functions is not very large, but the magnitude of the functions is quite small, which points to a potential issue. Due to the energy spacing in the data (0.5 meV for 55 meV data, 1 meV for 160 meV data, and 2 meV for the other incident energies), the sheer volume of data meant that the UMC procedure could not be carried out directly. Because of this, a replacement for the weighting function in Eq. 2.74 was required. Previously, this value has been too large, there have been a couple of recommended options [22]. The options include: verifying that the simulation model can sufficiently describe the data, labeling certain experimental data points as ‘questionable’ and enhancing their specific uncertainties, or spreading the discrepancy across all data points equally. This work chose the latter of the options, as there were many data points that were found to be discrepant, and changing the model would be infeasible.

The framework was run twice; once varying the parameters by 5% each, and then by varying the parameters by the amounts given from applying UMC to those results. The first step was done to determine the range of TIP4P/2005f parameters values that would constitute ‘good’ values to vary the parameters in UMC-B. The values from the first step, where the parameters are varied by 5%, are listed below in Table 2.

Table 2. TIP4P/2005f parameters – First Iteration

Parameter (units)	Value	St. Dev	St. Dev (%)
D_r (kJ/mol)	4.3603E+02	1.4054E+01	3.22
β (1/nm)	2.2782E+01	6.6308E-01	2.91
b_o (nm)	9.7271E-02	1.9630E-03	2.02
K_θ (kJ/(mol radian ²))	3.8473E+02	1.5365E+01	3.99
θ_o (degrees)	1.1000E+02	1.2489E+01	11.35
ε (kJ/mol)	7.9519E-01	1.6829E-02	2.11
σ (nm)	3.2146E-02	6.4887E-04	2.01
d_o (nm)	1.5765E-03	4.1663E-05	2.64

These values were then used as a prior for the second iteration of the framework, where the parameters were perturbed based on the standard deviations in Table 2. With this implementation, a further restriction was applied; of the 3464 simulations that ran to completion, only 60 reasonable results for property quantities of interest of light water (density, relative static dielectric constant, isothermal compressibility, dipole moment, and diffusion coefficient). Of these 5, the most important for the purpose of thermal scattering is the diffusion coefficient. This is because the diffusion coefficient is calculated directly from the frequency distribution, which is the primary input for calculating the intermediate structure factor from Eq. 2.66.

3.3 Results

3.3.1 TIP4P/2005f Parameters and Properties

First, the UMC method was used to determine what the updated potential values for the TIP4P/2005f model should be. These new results and uncertainties are shown in

Table 3, along with the original parameters of the TIP4P/2005f potential (from Table 1) and its percent difference from the original values. A plot of the distribution of these parameters is shown in Figure 6. The correlation matrix of the parameters is also calculated, according to Eq. 3.4

$$C_{i,j} = \frac{V_{i,j}}{\sqrt{V_{i,i}V_{j,j}}}, \quad (3.4)$$

where $V_{i,j}$ is the covariance matrix as defined by Eq. 2.76. The correlation matrix is shown instead of the covariance matrix in order to better convey the changes without having to take into magnitude of the values of the parameters, as would be in a covariance matrix. This correlation matrix is shown in Table 4. Since the correlation matrix, by definition, is symmetric, only the lower triangular portion of the matrix is shown.

Table 3. Results of UMC on TIP4P parameters

Parameter (units)	Value	St. Dev	St. Dev (%)	Original Value	Pct. Diff. (%)
D_r (kJ/mol)	4.363E+02	1.056E+01	2.42	4.326E+02	0.85
β (1/nm)	2.293E+01	4.975E-01	2.17	2.287E+01	0.26
b_o (nm)	9.593E-02	8.456E-04	0.88	9.419E-02	1.85
K_θ (kJ/(mol radian ²))	3.837E+02	1.213E+01	3.16	3.678E+02	4.31
θ_o (degrees)	1.052E+02	1.097E+01	10.42	1.074E+02	-2.02
ϵ (kJ/mol)	7.983E-01	1.752E-02	2.19	7.749E-01	3.02
σ (nm)	3.202E-02	2.913E-04	0.91	3.164E-02	1.20
d_o (nm)	1.581E-03	3.617E-05	2.29	1.546E-03	2.25

Almost every percent standard deviation of the values in Table 3 decrease from those in Table 2, with the exception of the potential well in the Lennard Jones potential ϵ . The large uncertainty on the equilibrium scattering angle θ_0 may indicate how insensitive it is in thermal scattering. This is backed up by the fact that, between various other potential models for water (TIP3P, SPC, etc.) the scattering angle can vary from 104.52° - 109.47° [28]. The values shown in Table 3 don't vary significantly from the original, which is to be expected, as the original TIP4P/2005f potential was used to calculate the ENDF8/B-VIII.β3 thermal scattering cross sections for light water [10], meaning they should already be good values. It is interesting that, for 7 of the 8 parameters, the updated value is greater than the original value, though there is no clear reason why this is the case.

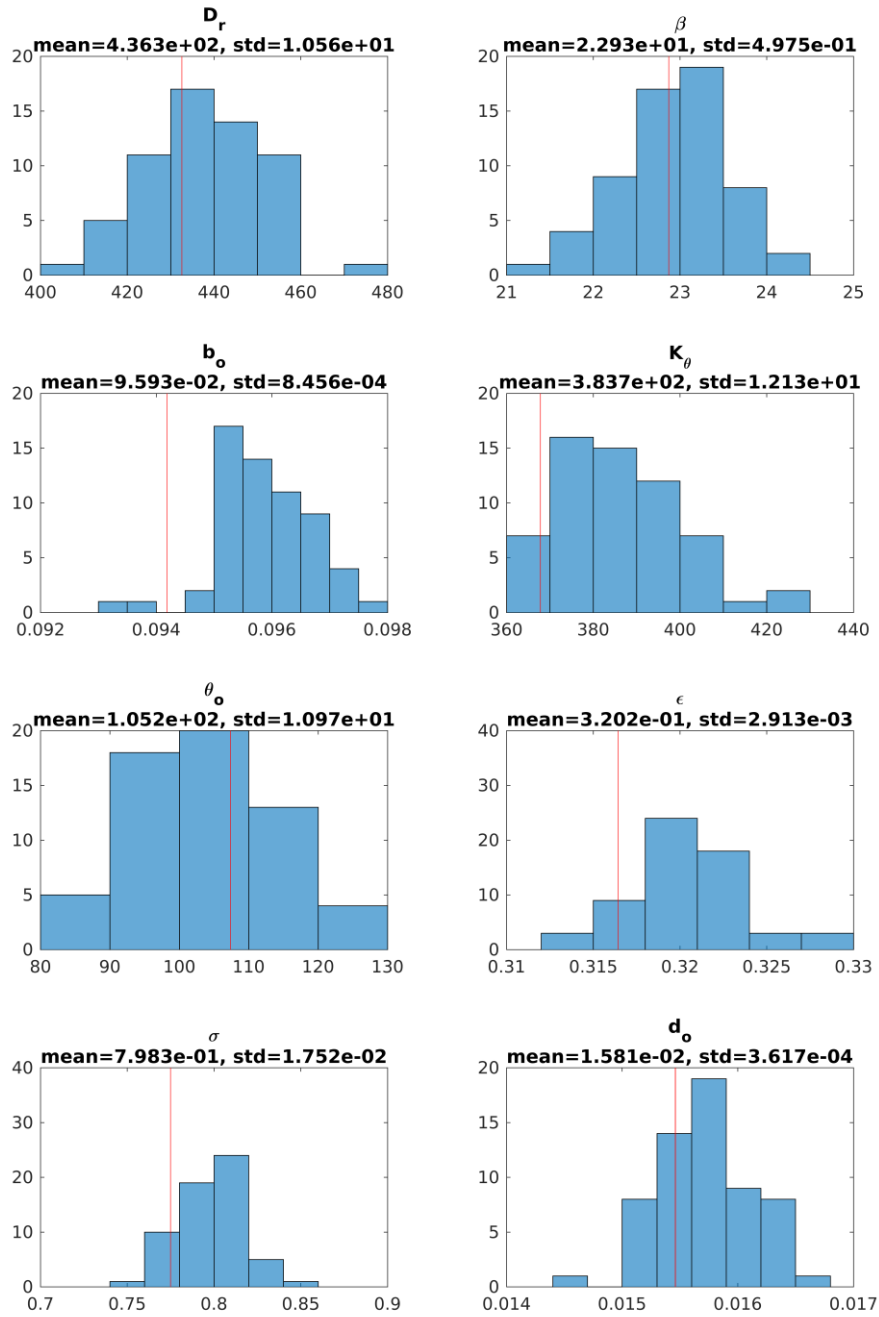


Figure 6. Distribution of TIP4P/2005f parameters. The red line is the value originally reported in Table 2.

The distribution of the parameter is mostly Gaussian, which is to be expected, as the parameters were sampled using a Gaussian distribution. One of the interesting outliers is how the distance from the hydrogen and oxygen molecule, b_o , appears to be decently larger than the published value. There are other parameters (namely K_θ) that differ by a wider margin than b_o , but the fact that only 2 simulations produced values smaller than the experimental value of the hydrogen-oxygen distance is interesting.

Table 4. Correlation Matrix of TIP4P Parameters from UMC

Parameter	D_r	β	b_o	K_θ	θ_o	ϵ	σ	d_o
D_r	1.000							
β	-0.180	1.000						
b_o	-0.052	0.177	1.000					
K_θ	0.091	0.022	0.056	1.000				
θ_o	0.143	-0.039	0.179	0.092	1.000			
ϵ	-0.237	0.115	0.475	-0.054	-0.714	1.000		
σ	-0.057	0.008	-0.037	-0.036	-0.092	0.003	1.000	
d_o	0.032	0.059	0.396	-0.139	-0.163	0.265	-0.128	1.000

The correlation matrix reveals some interesting properties of the TIP4P potential. There is a strong inverse correlation between the equilibrium angle θ_o and the depth of the potential well in the Lennard Jones potential ϵ , which is not inherently obvious by inspecting the formula. Additionally, there is almost no correlation between the potential well ϵ and the distance between particles σ . This is especially odd, as they are both in the same equation for the Lennard Jones potential in Eq. 2.78. When combined with the fact that the potential well ϵ had a jump in percent standard deviation as previously discussed, this may point towards an issue with the value assigned to this specific parameter.

In addition to the TIP4P parameters, the properties mentioned before were calculated using the UMC-B method. These results are shown in Table 5 with a plot of the distribution of these properties in Figure 7. The biggest differences come from the dipole moment and relative static dielectric constant. While these disagreements are quite large compared to the experimental values, this is expected when using the TIP4P/2005f potential, as shown in Table 6 [26]. Comparing the two tables, the UMC results give better agreement for the dipole moment, relative static dielectric constant, and diffusion coefficient by noticeable margins. The UMC analysis does do worse than the original in calculating density and isothermal compressibility, but not by excessively large margins.

Table 5. Result of UMC analysis on various properties

Property (units)	Value	St. Dev	St. Dev (%)	Exp. Value	Pct. Diff. (%)
Dipole moment (Debye)	2.371E+00	4.237E-01	17.87	2.950E+00	-19.63
Relative static dielectric constant (N/A)	7.181E+01	4.454E+01	62.03	7.840E+01	-8.41
Density (g/cm ³)	9.750E+02	1.899E+01	1.95	9.970E+02	-2.21
Diffusion Coefficient	2.247E+00	6.406E-02	2.85	2.270E+00	-1.03
Isothermal Compressibility	4.697E-01	3.350E-02	7.13	4.530E-01	3.69
Temperature (K)	2.985E+02	3.283E+00	1.10	2.980E+02	0.16

Table 6. Properties from TIP4P/2005f potential at 298 K

Property (units)	Value	Exp. Value	Pct. Diff. (%)
Dipole Moment (Debye)	2.319E+00	2.950E+00	-21.39
Relative static dielectric constant (N/A)	5.530E+01	7.840E+01	-29.46
Density (g/cm ³)	9.977E+02	9.970E+02	0.07
Diffusion Coefficient	1.930E+00	2.270E+00	-14.98
Isothermal Compressibility	4.460E-01	4.530E-01	-1.55

Regarding the distribution of properties shown in Figure 7, the dipole moment, isothermal compressibility, and temperature appear to follow a Gaussian distribution, while the relative static dielectric constant, density, and diffusion coefficient do not. The dielectric constant and density appear to follow more of a beta distribution, though the reason for why they do is unclear. In addition, there doesn't appear to be any sort of distribution that the diffusion coefficient follows, which does not make intuitive sense. This warrants future investigation into why these properties appear to follow their respective distributions.

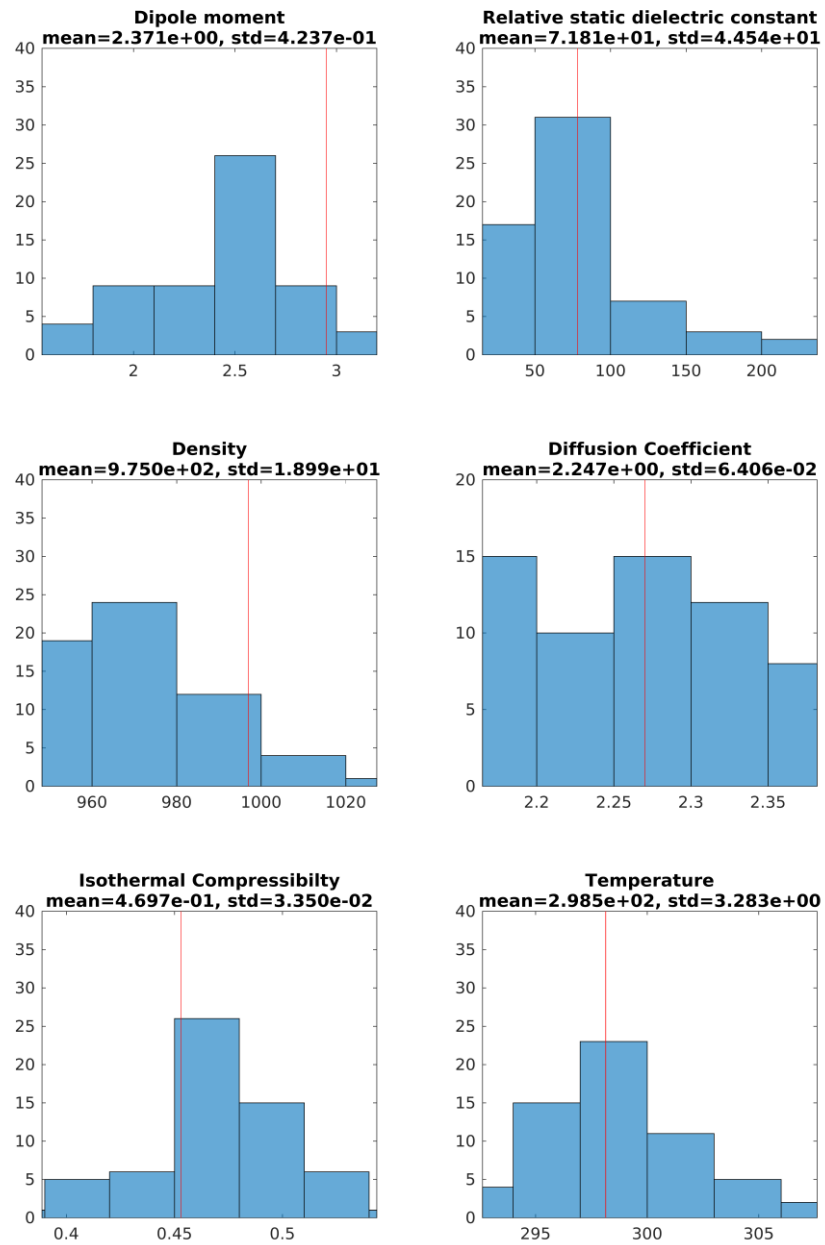


Figure 7. Distribution of properties.

3.3.2 *Double Differential Cross Section*

As a first step of validating the new thermal scattering data, they are plotted against the experimental data from the SNS, which can be found in APPENDIX A. In these plots, the green band represents the simulation data ± 1 standard deviation away from the mean value. These were created by perturbing the mean DSF by the uncertainty of the DSF multiplied by either ± 1 . Unfortunately, this is synonymous to assuming that the correlation matrix is a full matrix of ones, which is not true. The alternative would be to randomly vary the individual values of the DSF by their uncertainties, which implies a correlation matrix of ones along the diagonal and zeros elsewhere. Doing this, however, yields unphysical results that cause NJOY to break. Because of this, the full correlation matrix is assumed for now until a better covariance matrix can be calculated. The data were generated by running a simplified MCNP model meant to recreate the SEQUOIA detector, with the detector resolution function applied afterwards.

Overall, the simulation results seem to agree favorably with the ENDF/B-VIII.β3, which makes sense since the same molecular dynamic code and light water model was used for both. The differences come about from the modification of the parameters made in this work. There are a couple of weird quirks in the data that should be mentioned. In the 55 meV data plots, the experimental results at 35° disagree significantly with the simulation results, which contrasts the general agreement they've shown in the other scattering angles. This is most likely due to an error in the data, as the results at 34° and 36° agree much more favorably. Another instance occurs with the 160 meV plot at 35° , where there is an odd indentation at the peak of the experimental data which is also not exhibited at 34° and 36° .

Additionally, the thermal scattering data is plotted against independently gathered experimental data [29]. The data from this source did not include any uncertainties, so no attempt is made to assume what they may be here. The plots of these cross sections are shown in Figure 8 and Figure 9. Both of these sets have simulation data that are convoluted with a Gaussian resolution function to best approximate the detector resolution function. The 151 meV data assumes a Gaussian function with $\sigma=7$ meV, and the 304 meV data has $\sigma=9.6$ meV. As with the SNS data set, the simulation data appears to agree with both the ENDF/B-VII.1 and ENDF/B-VIII.β3 data. All sets of these data, however, appear to diverge from the experimental results at scattering angles greater than 90° , which corresponds to a back-scattering event. This may point to a slight deficiency in how the underlying theoretical models handle back-scattering.

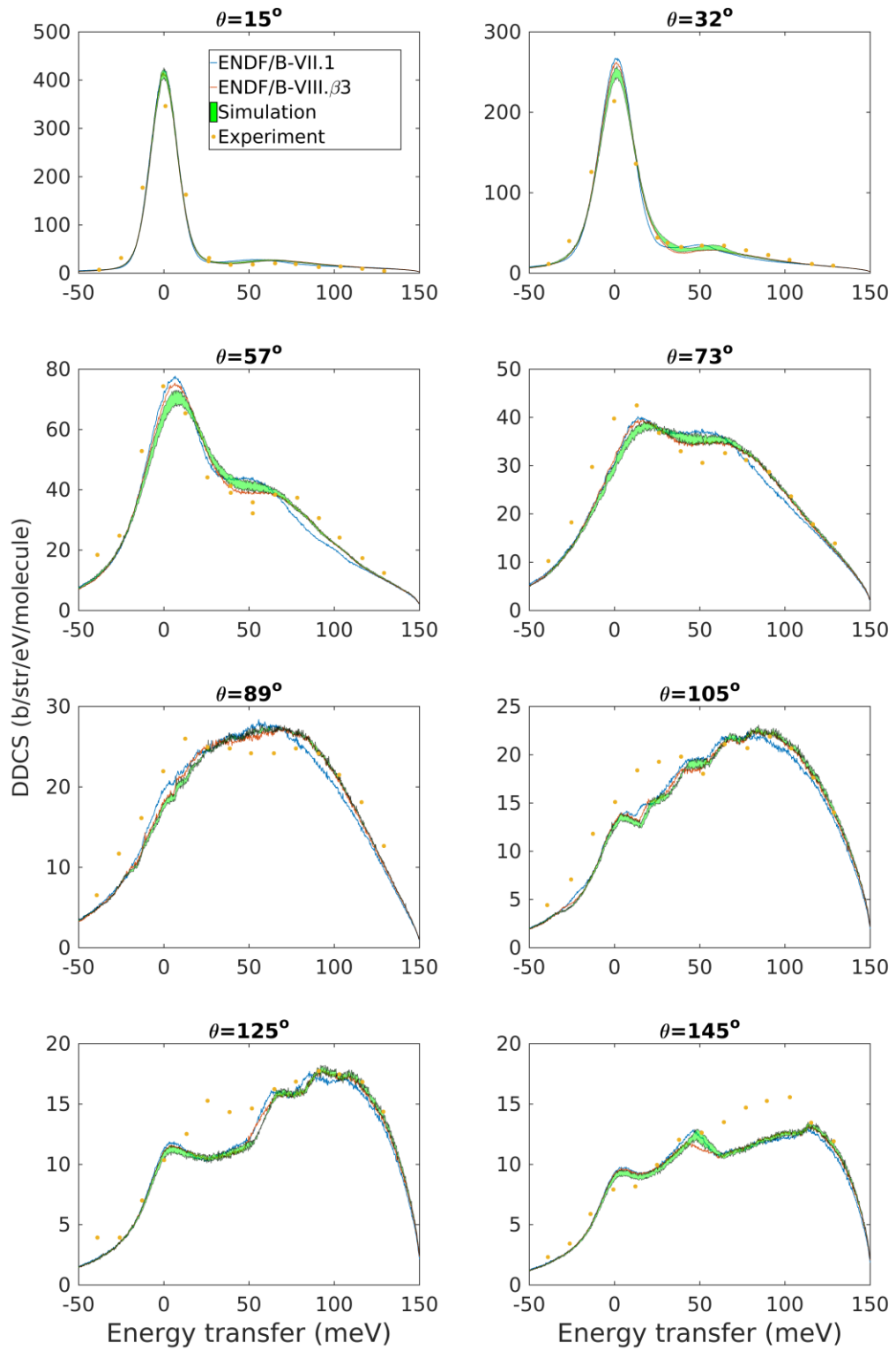


Figure 8: DDCS plot with incident energy of 151 meV and scattering angles between 15°-145°

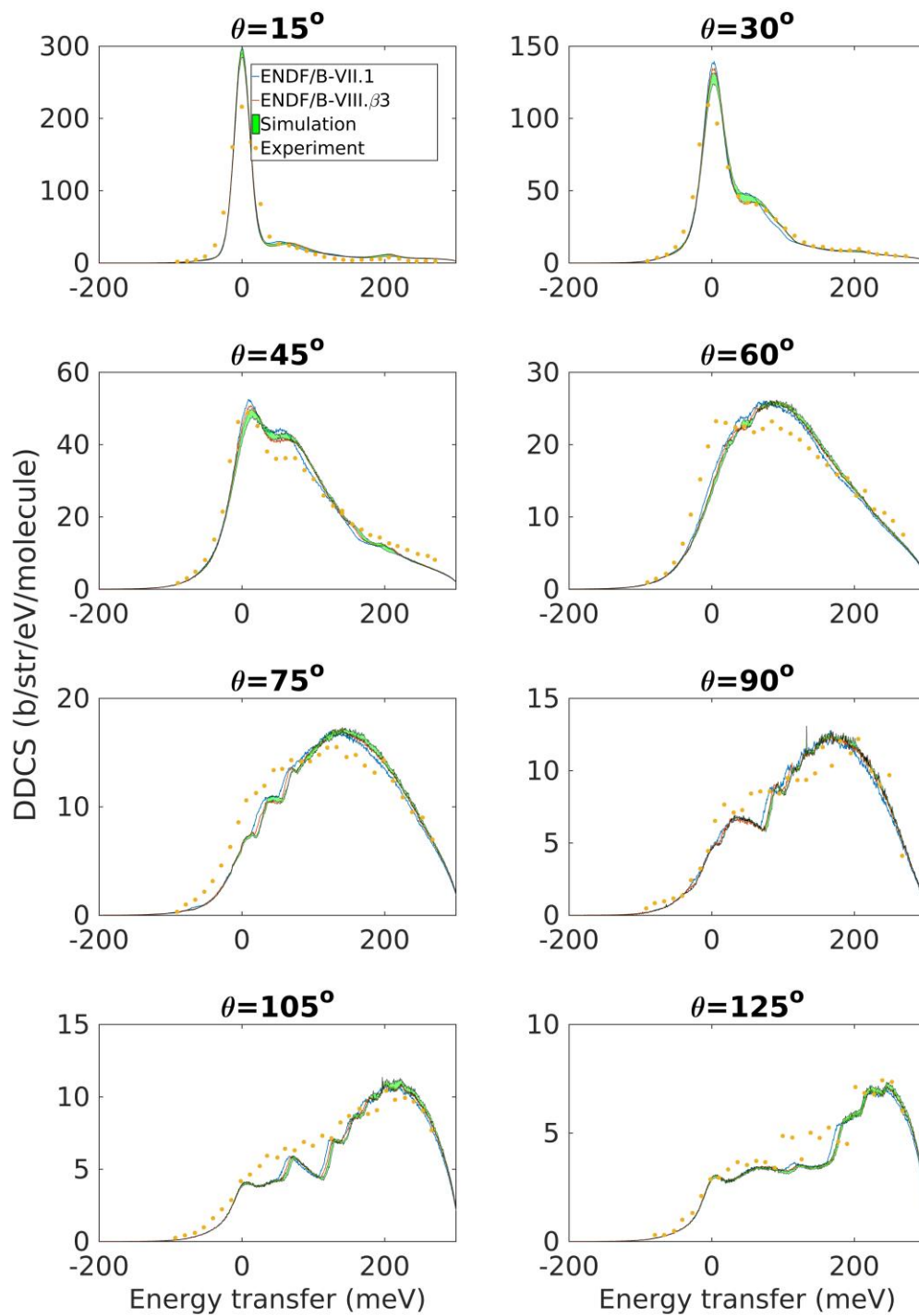


Figure 9: DDCS plot with incident energy of 304 meV and scattering angles between 15° - 125°

3.3.3 Total Cross Section

Finally, the total cross section was plotted against several other experimentally gathered cross sections [30] [31] and is plotted in Figure 10. As with the DDCS in the previous section, the green band represents the simulation data ± 1 standard deviation away from the mean value. Here, however, the uncertainties were calculated using two different methods. The first method (Method 1) was calculated by perturbing the mean DSF by the uncertainty of the DSF multiplied by either ± 1 and calculating the total scattering cross section. The second method (Method 2) uncertainties were generated by applying the UMC-B method of directly on the total scattering cross section (using the UMC-B weights that were previously calculated with the DDCS), finding its associated mean and uncertainty, then perturbing the mean total cross section by the uncertainty of the total cross section multiplied by either ± 1 . In both methods, the absorption of hydrogen and the total oxygen cross section were added.

Overall, the simulation results for the first method are slightly less accurate at low energies (less than 1 meV) compared against the ENDF/B-VIII.β3 results. The simulation results are also noticeably larger than both ENDF results in the 1-10 meV range. This is particularly strange, as the double differential cross sections seem to agree favorably with the ENDF results. The results from Method 2, however, are noticeably better than the Method 1 results. Specifically, the low-energy region agrees more favorably with the experimental data, and the uncertainties in Method 1 are significantly larger than the uncertainties in Method 2.

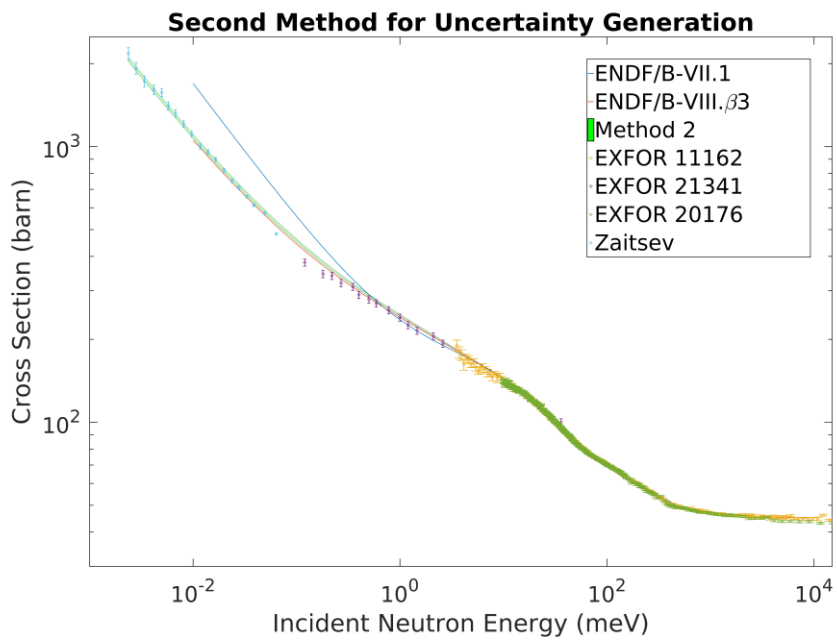
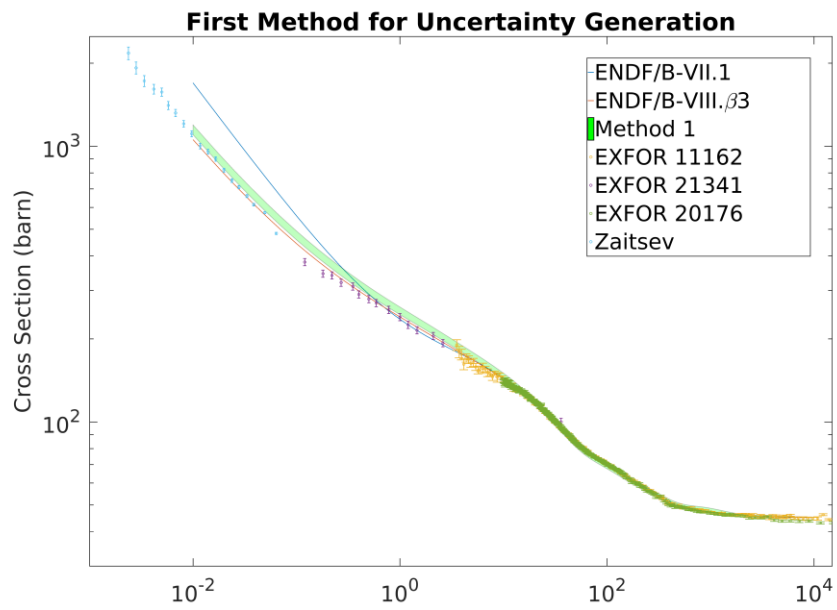


Figure 10. Total cross section of light water for both methods of uncertainty generation.

To understand why there are such significant differences between the simulation results and ENDF results, a plot of the normalized DSF is shown in Figure 11, where the top plot has a linear y-axis and the bottom plot has a logarithmic y-axis. It is clear that, the further from the peak the structure factors get, the more they diverge. Specifically, the simulation results appear to be larger than the ENDF/B-VIII.β3 results. This is most likely due to the method which is used to calculate the DSF. The ENDF (both ENDF/B-VII.1 and ENDF/B-VIII.β3) libraries were evaluated using NJOY, which uses the phonon expansion to calculate the DSF. The simulation results use a more direct approach involving explicitly calculating the intermediate structure factor, then using the full Fourier transform to calculate the DSF. The full Fourier transform is used instead of a fast Fourier transform because the spacing in time is not linearly spread out.

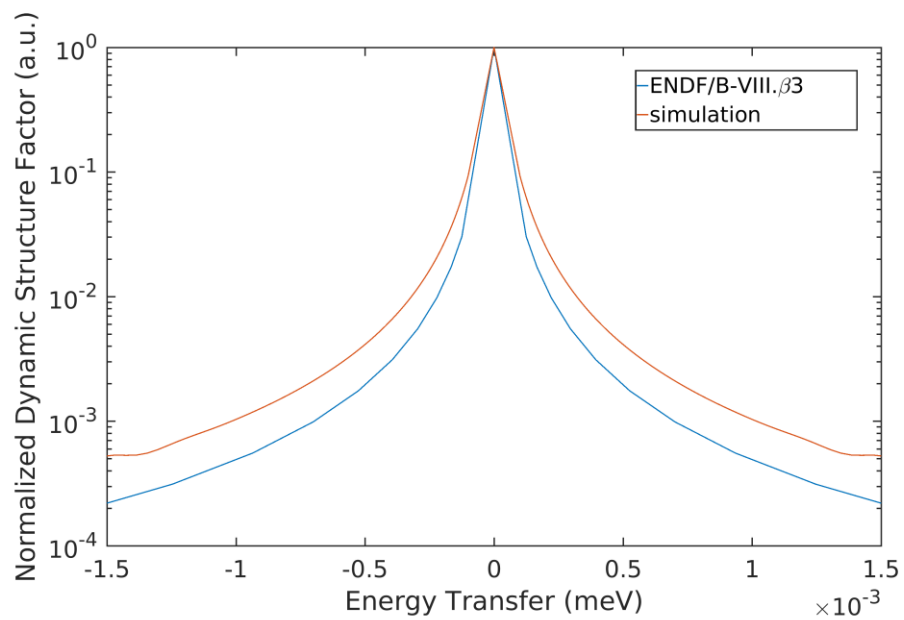
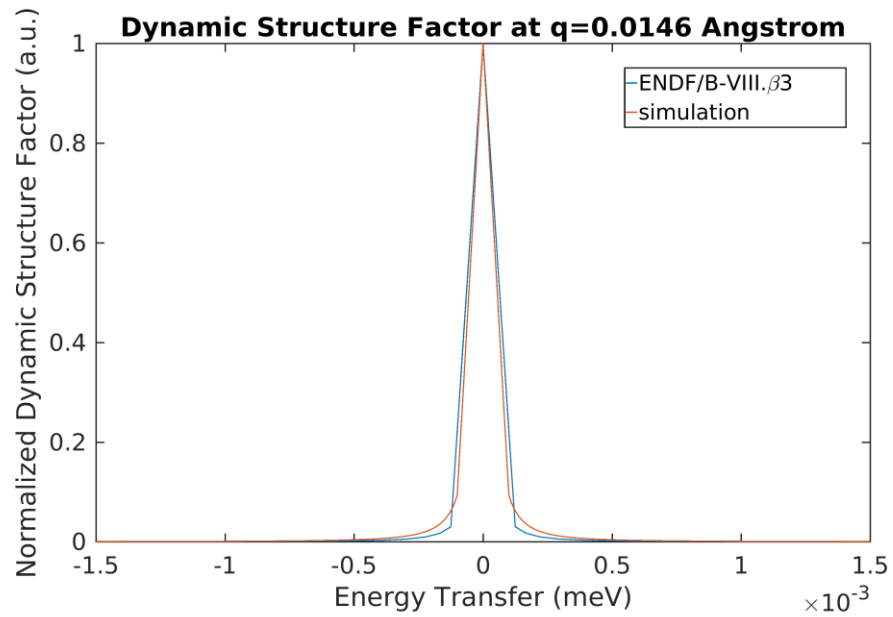


Figure 11. Comparison of DSFs

CHAPTER 4. BENCHMARKS

As a second method for validating these new cross sections, three benchmark problems were selected from the International Handbook of Evaluated Criticality Safety Benchmark Experiments (ICSBEP) [32]. The benchmarks were chosen using the Database for the International Handbook of Evaluated Criticality Safety Benchmark Experiments (DICE) software [33]. The three problems selected were the PU-SOL-THERM-033-003 (PST-033-003), LEU-COMP-THERM-079-007 (LCT-079-007), and HEU-COMP-THERM-006-003 (HCT-006-003) benchmarks. The benchmarks were chosen specifically to encompass several different fuel types (plutonium, low enriched uranium, and high enriched uranium) in the thermal energy range, as well as covering different sensitivities to k_{eff} based on perturbations in the ^1H cross section. A plot of these sensitivities as a function of energy is shown below in Figure 12. The sensitivities were generated using SCALE [34].

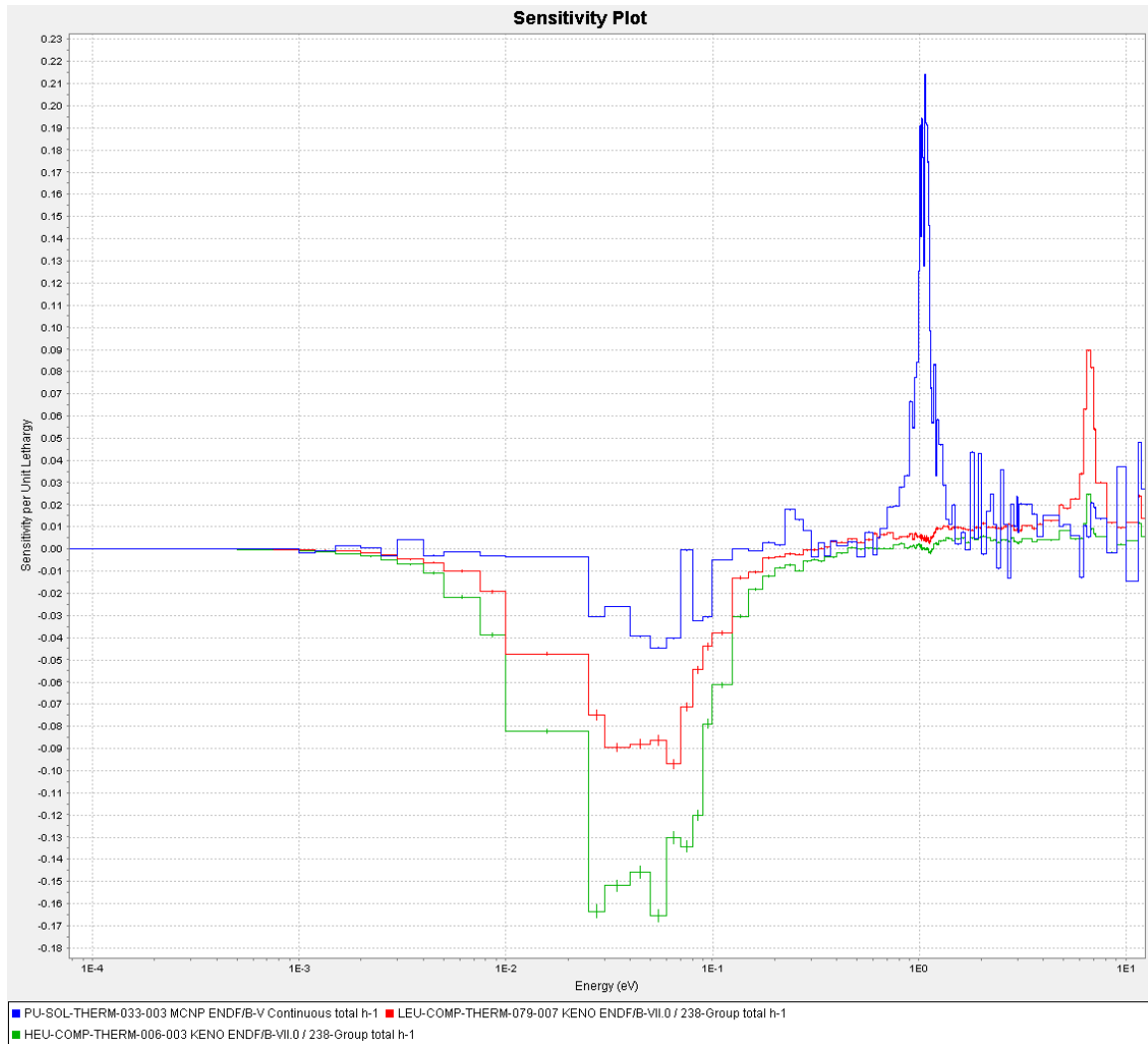


Figure 12. Sensitivity plot of k_{eff} for ICSBEP benchmark problems.

4.1 Benchmark Descriptions

4.1.1 PST-033-003

The PST-033-003 benchmark is based on a plutonium nitrate solution. The experiments were carried out in 1966-1968 in Valduc, France. The purpose of the experiments was to provide criticality data on plutonium nitrate solutions poisoned with borated tubes or Rashig rings. This specific experiment, however, was meant to be a

benchmark, and therefore had neither the borated tubes nor the Rashig rings. This both simplifies the geometry of the problem, as well as the total material composition of the problem. The concentration of ^{240}Pu and concentration of plutonium in the solution were varied, and the inner and outer tanks were filled until criticality was reached (within 0.1%). Based on the height of liquid, the critical height was extrapolated. The plutonium solution was placed in a 36 cm. diameter inner tank with a water reflector surrounding the inner tank. The water was contained in an outer tank with diameter of 110 cm. A XZ view of the model is shown in Figure 13, and a XY view of the model is shown in Figure 14. Material compositions for the model are shown given in Table 7.

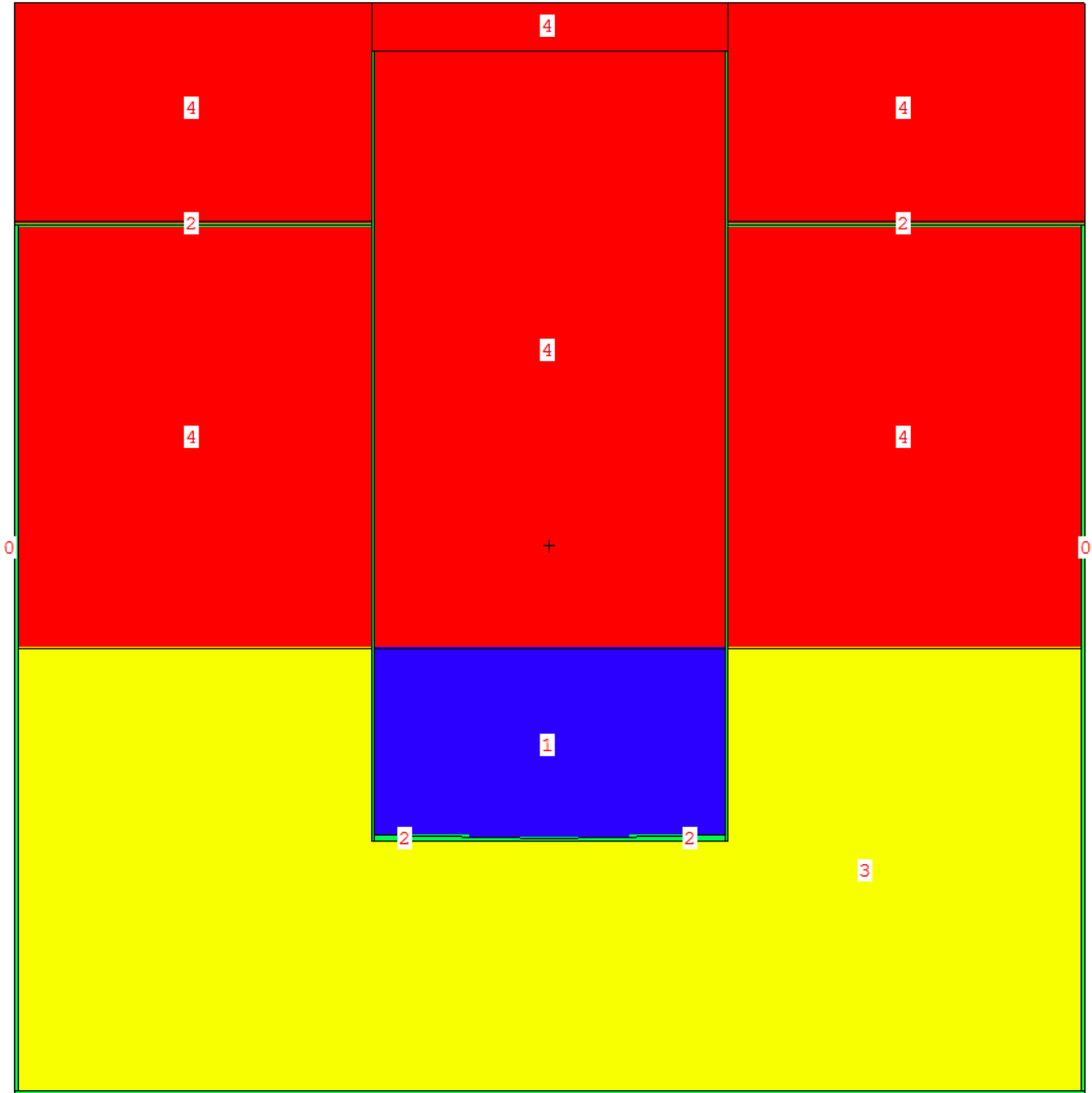


Figure 13. XZ view of the PST-033-003 benchmark. The numbers correspond to material labels detailed in Table 7.

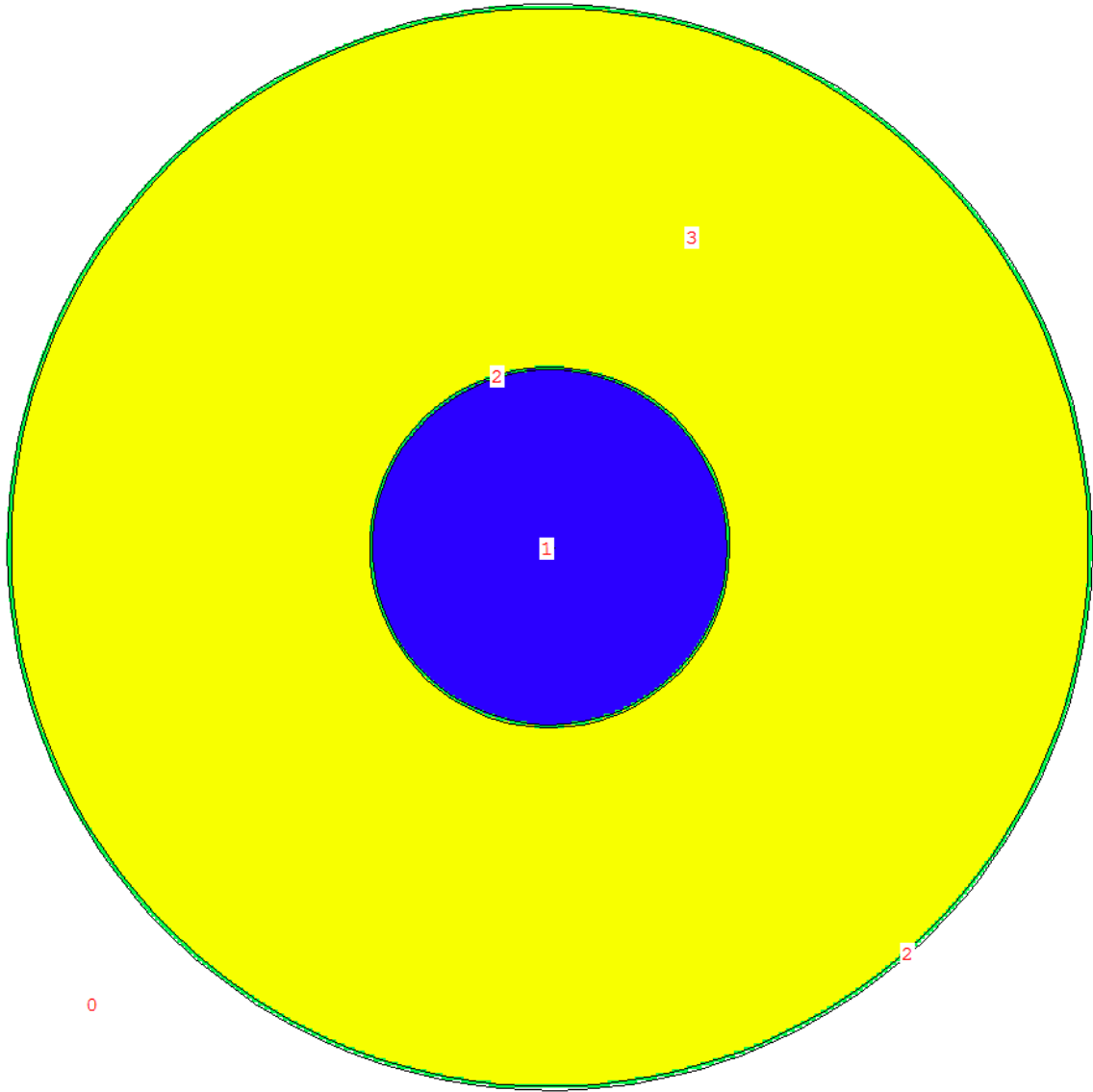


Figure 14. XY view of the PST-033-003 benchmark. The numbers correspond to material labels detailed in Table 7.

Table 7. Material Specifications for PST-033-003

Material	Number	Color	Density (g/cm ³)	Element / Isotope	Atom Number Density (barn ⁻¹ cm ⁻¹)
Plutonium Nitrate Solution	1	Blue	1.5629	²³⁵ U	2.2089E-10
				²³⁸ U	3.0939E-08
				²³⁹ Pu	7.3203E-04
				²⁴⁰ Pu	2.3622E-05
				²⁴¹ Pu	9.0055E-07
				²⁴² Pu	8.9683E-08
				²⁴¹ Am	1.0506E-07
				H	5.4569E-02
				O	4.0095E-02
				N	4.5129E-03
				Fe	4.4211E-06
				Cr	5.2188E-07
				Ni	6.1647E-07
				Mn	1.9757E-07
				Ca	2.7083E-06
Cu	3.7009E-07				
Mg	1.4886E-06				
Zn	4.1498E-07				
Na	1.9672E-06				
Stainless Steel	2	Green	7.9	Fe	5.9546E-02
				Cr	1.6469E-02
				Ni	8.1061E-03
				Mn	8.6597E-04
				Si	1.6939E-03
				S	4.4504E-05
				P	6.1439E-05
C	1.1883E-04				
Air	3	Red	0.001225	N	4.1985E-05
				O	1.1263E-05
Water	4	Yellow	0.99777	H	6.6706E-02
				O	3.3353E-02

The experimental criticality was found to be 1.000. There are no biases for the benchmark problems, but there are several sources of experimental uncertainties. Uncertainties in the temperature of the solution account for 16 pcm, while uncertainties in the acidity, plutonium concentration, iron concentration, density, and isotopic concentrations of ^{239}Pu and ^{241}Am account for an additional 140 pcm of uncertainty, geometric uncertainties add 52 pcm, and uncertainties about the composition of the stainless steel give 55 pcm. These uncertainties lead to a benchmark-model criticality of 1.000 ± 0.00162

4.1.2 LCT-079-007

The LCT-079-007 experiment was designed investigate the effect of fission product materials on critical systems. It was a part of the Burnup Credit Critical Experiment (BUCCX), and consists of water-moderated and water-reflected array of Zircaloy-clad triangular pitched UO_2 fuel elements spaced 2.8 cm apart. These experiments were carried out in 2002 at Sandia National Laboratory. The approach-to-critical experiment was done by varying the number of integral fuel elements in the array until criticality was reached. This specific experiment contained 131 fuel elements, but the extrapolated critical array size was found to be 131.959 ± 0.018 elements, so 132 fuel elements are used in the model. The core consists of 91 driver fuel elements, 3 control and safety elements, 1 source element at the center, and 36 experimental elements. A XZ view of the model is shown in Figure 15, and a XY view of the model is shown in Figure 16. Material compositions for the model are shown given in Table 8.

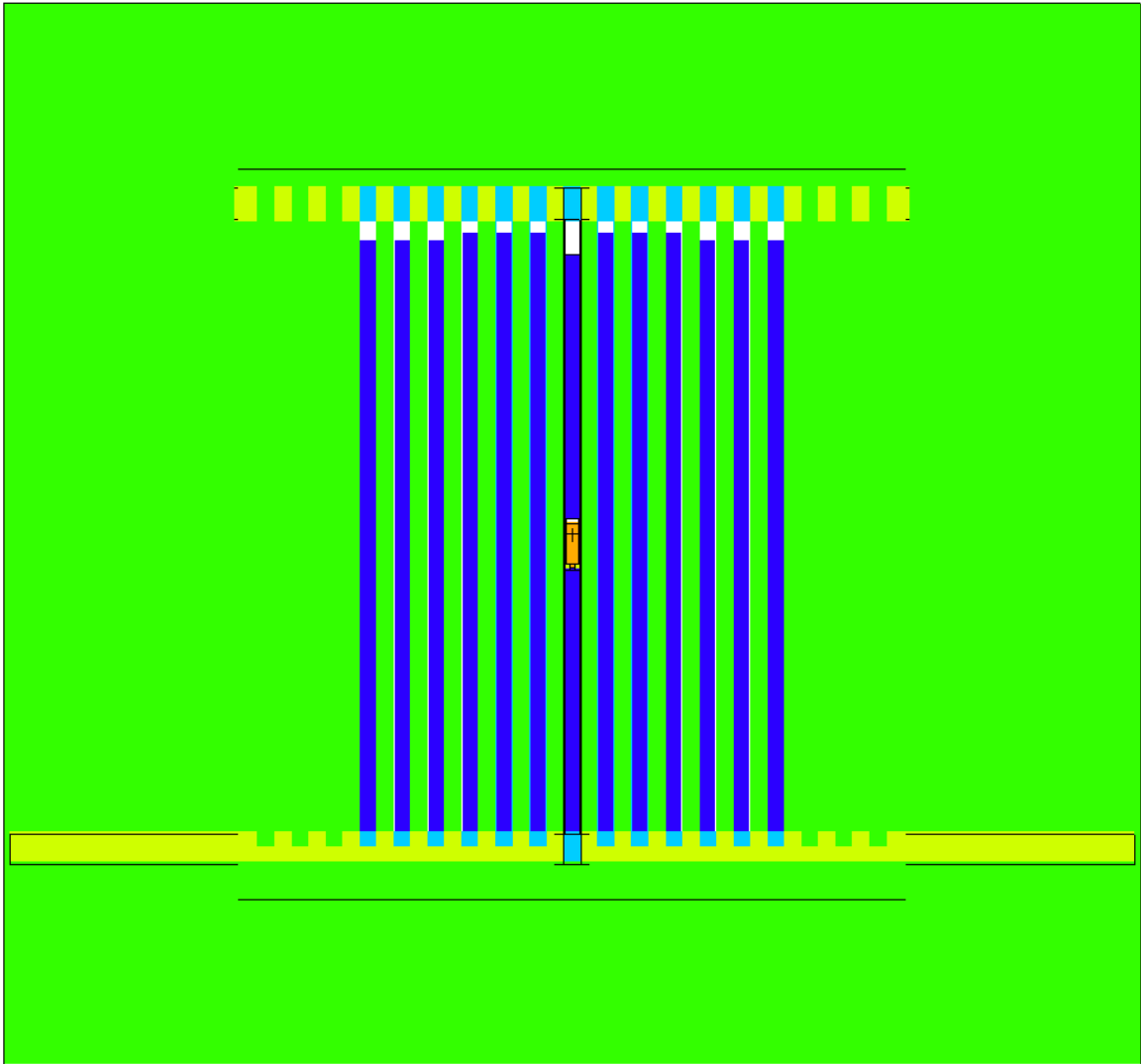


Figure 15. XZ view of the LCT-079-007 benchmark. The material labels are left off for convenience, but the colors correspond to the materials detailed in Table 8.

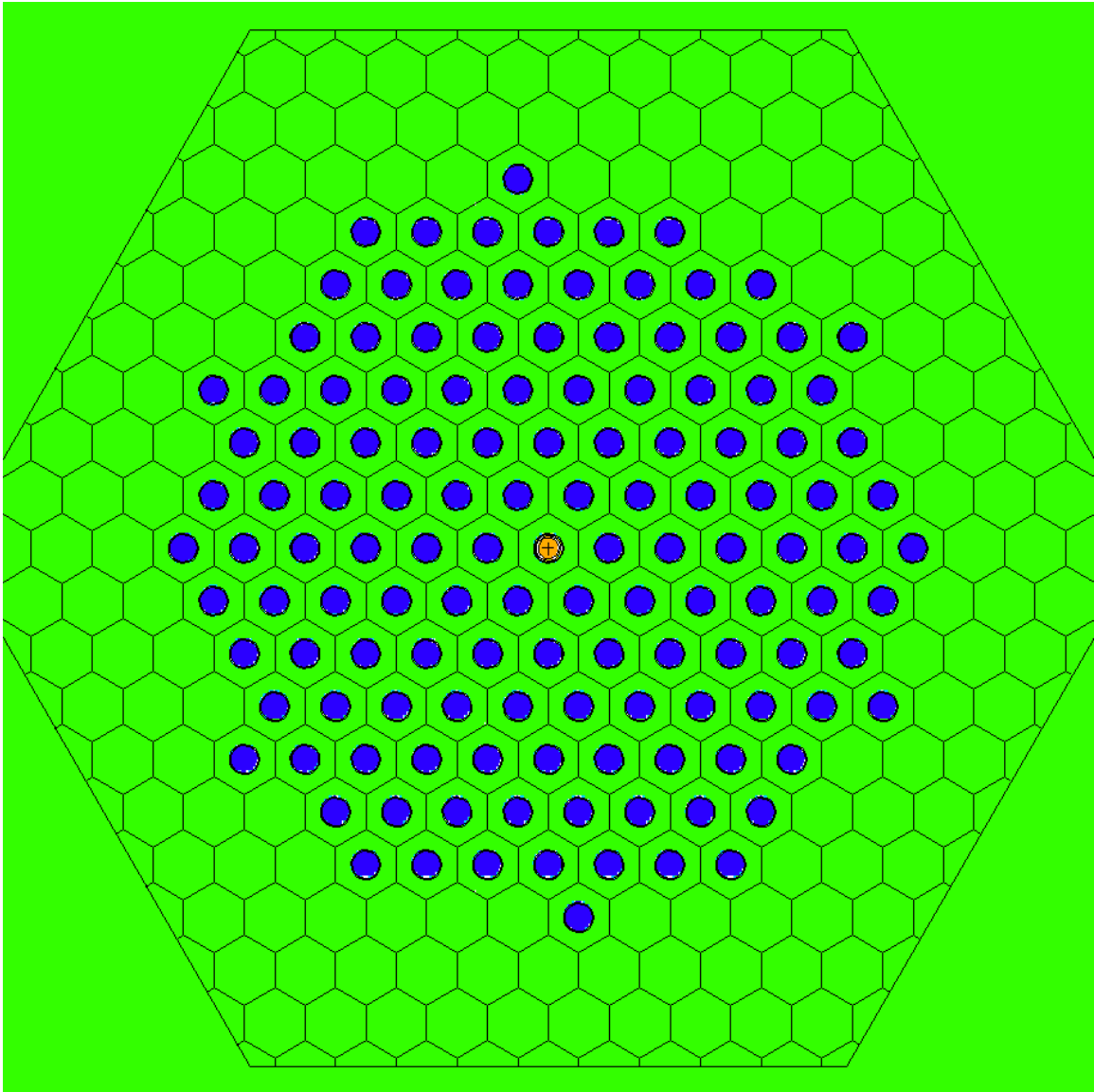


Figure 16. XY view of the LCT-079-007 benchmark. The material labels are left off for convenience, but the colors correspond to the materials detailed in Table 8.

Table 8. Material Specifications for LCT-079-007

Material	Number	Color	Density (g/cm ³)	Element / Isotope	Atom Number Density (barn ⁻¹ cm ⁻¹)
UO2 Fuel	1	Blue	10.49	²³⁴ U	5.1985E-06
				²³⁵ U	1.0132E-03
				²³⁶ U	5.1544E-06
				²³⁸ U	2.2221E-02
				O	4.6888E-02
Zircaloy-4	2	Teal	6.55	Zr	4.2425E-02
				Sn	4.8181E-04
				Fe	1.4832E-04
				Cr	7.5862E-05
				O	3.0818E-04
Water	3	Green	0.996556	H	6.6625E-02
				O	3.3313E-02
6061 Aluminum	4	Beige	2.7	Al	5.9015E-02
				Cr	6.0979E-05
				Cu	7.0365E-05
				Mg	6.6899E-04
				Si	3.4736E-04
304 Stainless Steel	5	Orange	7.9	Fe	5.9632E-02
				Cr	1.7384E-02
				Ni	7.7008E-03
				Mn	8.6597E-04
				Si	8.4697E-04

The experimental criticality was found to be 1.0000. There are no biases for the benchmark problems, but there are uncertainties in both the experimental setup and the computational model simplification. The experimental uncertainties surrounding various material compositions and geometric configurations accounted for a total of 76 pcm of uncertainty. Additionally, there were several simplifications made to the computer

simulation model that resulted in changes to the criticality and its uncertainty. Various model changes, a minimal net change to the criticality of 0.00002 ± 0.00006 . The addition of the of another fuel element, which came about from rounding the number of elements so that the system could be critical, added 0.000077 ± 0.000027 to the criticality. The model also assumed the same fuel mass for all the elements, when the fuel mass in the drive and experimental fuel elements were slightly different from the other fuel element-containing components. Assuming that they all had the same fuel mass changes the criticality by 0.00018 ± 0.00005 . These combined give a benchmark-model criticality of 1.0003 ± 0.0008 .

4.1.3 HCT-006-003

The HCT-006-003 experiment is a water-moderated hexagonally pitched lattice with highly enriched ($\sim 80\%$ ^{235}U) cross-shaped fuel rods. These experiments were performed at the RRC Kurchatov Institute in 1994-1995. The critical configuration contains a uniform hexagonal lattice with a 21.13 mm pitch containing 554 fuel rods. The fuel rods have a cross-shaped cross section, and are twisted to form a spiral shape. The number of rods was selected such that the system would be critical when the top water reflector height was at least 200 mm. The assembly is configured in a circular area with a diameter of 528.25 mm. The assembly is contained in a 1.6 m diameter tank filled with water 2 m high. A XZ view of the model is shown in Figure 17, and a one-quarter view from the XY plane of the model is shown in Figure 18. Material compositions for the model are shown given in Table 9.

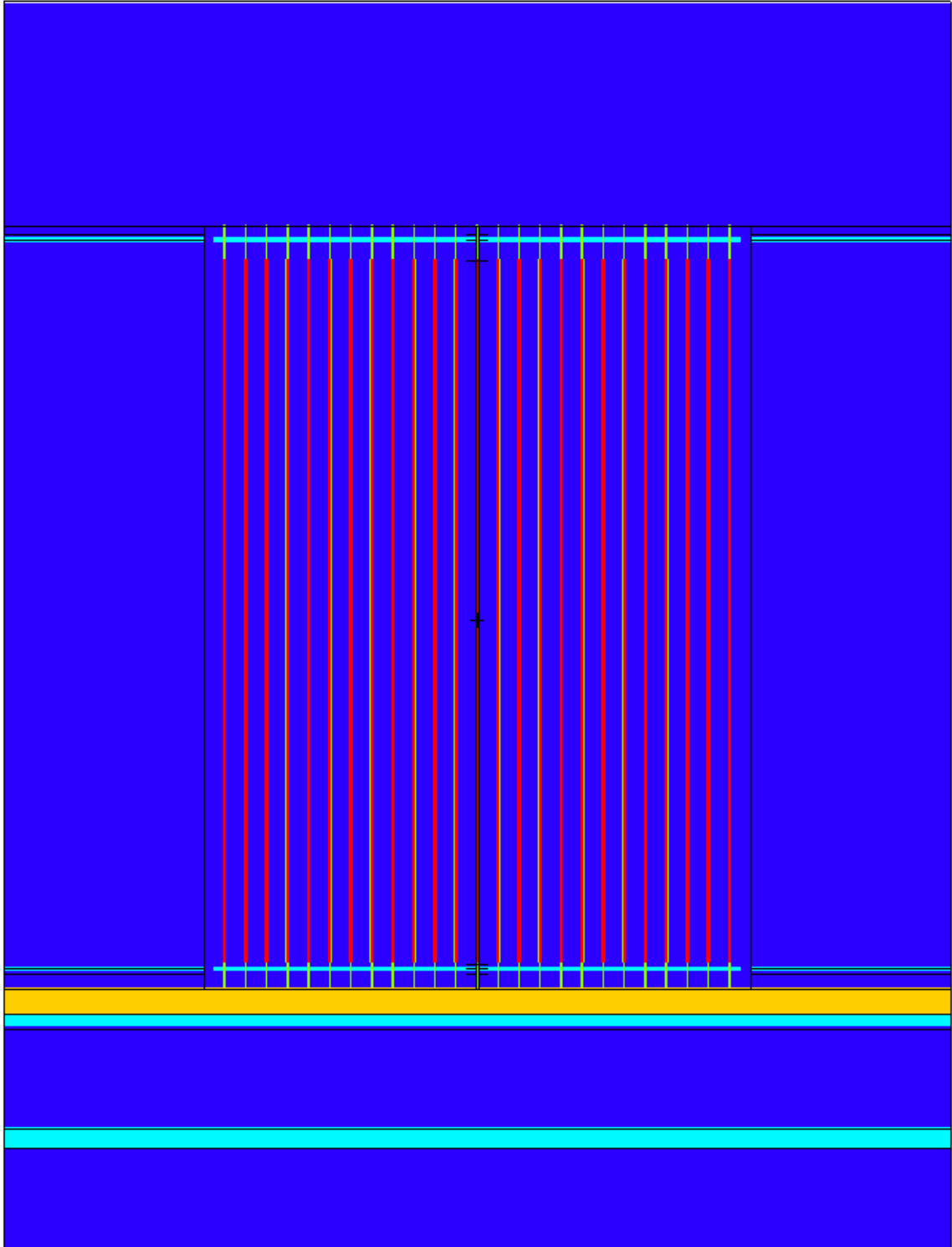


Figure 17. XZ view of the HCT-006-003 benchmark. The material labels are left off for convenience, but the colors correspond to the materials detailed in Table 9.

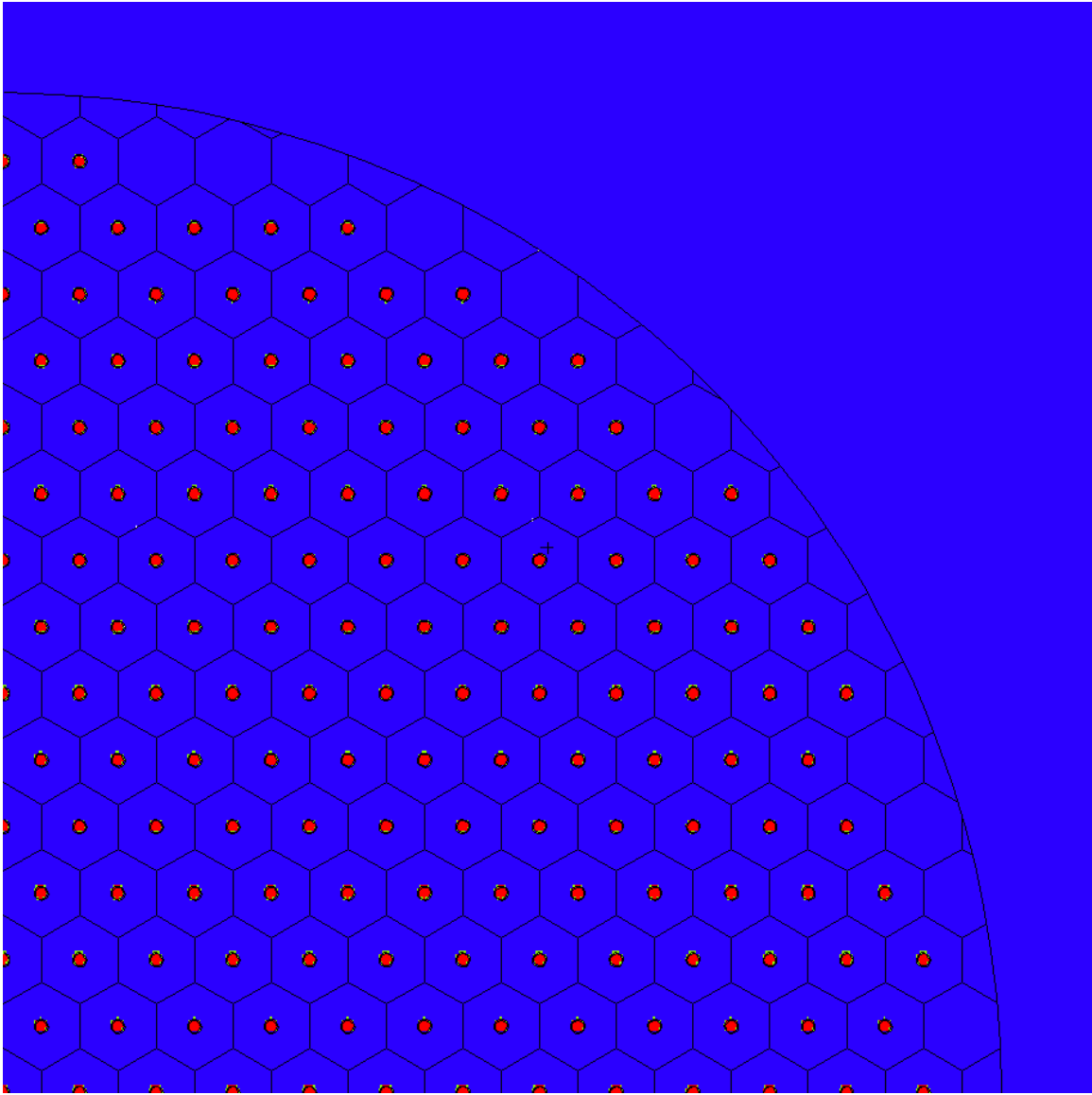


Figure 18 XY 1/4th view of the HCT-006-003 benchmark. The material labels are left off for convenience, but the colors correspond to the materials detailed in Table 9.

Table 9. Material Specifications for HCT-006-003

Material	Number	Color	Density (g/cm ³)	Element / Isotope	Atom Number Density (barn ⁻¹ cm ⁻¹)
Water	1	Dark Blue	0.9982	H	6.6736E-02
				O	3.3368E-02
Aluminum alloy AD1	2	Teal	2.71	Al	6.0062E-02
				Si	2.0337E-04
				Fe	8.7667E-05
				Cu	1.2841E-05
Stainless Steel	3	Green	7.9	C	3.5648E-04
				Si	1.3551E-03
				Cr	1.4639E-02
				Fe	5.4698E-02
				Ni	1.2159E-02
				Nb	4.6086E-04
Plexiglas	4	Yellow	1.18	Mo	1.4876E-03
				H	5.6826E-02
				O	1.4194E-02
Fuel	5	Red	8.1118	C	3.5486E-02
				²³⁴ U	5.3830E-05
				²³⁵ U	4.4208E-03
				²³⁶ U	1.2208E-05
				²³⁸ U	1.0627E-03
				O	1.1360E-02
				Cu	5.3437E-02

The experimental criticality was found to be 1.000. There are some uncertainties in the material composition and exact experimental setups that contribute to some uncertainties. Specifically, uncertainties in the pitch, fuel cross section area, and length account for 28 pcm uncertainty, while uncertainties in the fuel mass, enrichment, and clad mass contribute 44 pcm uncertainty to the criticality. For this framework, the simplified

model is used. The simplifications in this model mean that, instead of the cross-shaped fuel rods, cylindrical fuel rods are used. This introduced a bias in the criticality that reduced the criticality by 0.0231. The spiraling in the fuel rods was also removed for the model, but it was determined that this introduced a negligible difference in the criticality, and as such is ignored. The uncertainties mentioned before were also slightly increased in the simplified model to account for statistical uncertainties in the estimated change of the criticality. With these factors, the benchmark-model criticality was found to be 0.9769 ± 0.0049 .

4.2 Benchmark Results

To validate the new cross sections, the benchmarks were run using the ENDF/B-VII.1, and ENDF/B-VIII.β3 libraries as well as the new simulated cross sections. Since the uncertainties cannot be propagated through MCNP, the simulated data was perturbed by the simulated uncertainties and run. Specifically, the DSF was created by perturbing the mean DSF by the uncertainty of the DSF multiplied by either a normally distributed random number. This should give a rudimentary first approximation of the sensitivity of the system to thermal scattering cross sections. The simulations were all run using MCNP6.1, with each input being run such that the stochastic uncertainty would be 4 pcm. The results for the PST-033-003, LCT-079-007, and HCT-006-003 benchmarks are shown in Table 10, Table 11, and Table 12, respectively.

A general observation about all three benchmarks is that the simulation results show a greater k_{eff} than the ENDF/B-VII.1 or ENDF/B-VIII.β3 results. This can be attributed to

the fact that, as pointed out in the total cross section plot in Figure 10, the simulation cross section is greater than the either ENDF libraries below 10 meV. The benchmarks were originally chosen since they each exhibited a negative sensitivity to perturbations in the hydrogen cross section in the 1-100 meV range, and it was thought that

Table 10. PST-033-003 Results

ENDF Library	K_{eff}	St.Dev (pcm)	ΔK_{eff} (pcm)
Benchmark	1.00000	162	N/A
ENDF/B-VII.1	0.99349	4	651
ENDF/B-VIII.β3	0.99422	4	578
Mean	0.99483	4	517
Var. 1	0.99472	4	528
Var. 2	0.99471	4	529
New XS Var. 3	0.99482	4	518
Var. 4	0.99473	4	527
Var. 5	0.99467	4	533
Var. 6	0.99493	4	507

The PST benchmark shows that the simulation results get closer to the benchmark results, and they are not overly sensitive to thermal scattering, based on the change of eigenvalue between the maximum and minimum values (26 pcm). The difference between the ENDF/B-VIII.β3 and simulation results is 61 pcm, which is a greater difference than the previously mentioned 26 pcm range of the 6 variations to the cross sections.

Table 11. LCT-079-007 Results

ENDF Library	K_{eff}	St.Dev (pcm)	ΔK_{eff} (pcm)
Benchmark	1.00030	80	N/A
ENDF/B-VII.1	0.99933	4	97
ENDF/B-VIII.β3	0.99982	4	48
Mean	1.00006	4	24
Var. 1	1.00000	4	30
Var. 2	0.99995	4	35
New XS Var. 3	1.00026	4	4
Var. 4	1.00001	4	29
Var. 5	0.99961	4	69
Var. 6	1.00039	4	-9

The LCT benchmark results also show that the simulation results get closer to the benchmark results, but the ENDF/B-VIII.β3 and simulation results both fall within the standard deviation of the benchmark uncertainty, so it is not as meaningful as with the PST benchmark. Even with an eigenvalue difference of 78 pcm between the maximum and minimum variations, the varied simulations fall within the uncertainty of the benchmark.

Table 12. HCT-006-003 Results

ENDF Library	K_{eff}	St.Dev (pcm)	ΔK_{eff} (pcm)
Benchmark	0.97690	490	N/A
ENDF/B-VII.1	0.98190	4	-500
ENDF/B-VIII.β3	0.98232	4	-542
Mean	0.98245	4	-555
Var. 1	0.98235	4	-545
Var. 2	0.98222	4	-532
New XS Var. 3	0.98269	4	-579
Var. 4	0.98225	4	-535
Var. 5	0.98187	4	-497
Var. 6	0.98290	4	-600

The HCT results in show the simulation seems to do worse than the ENDF/B-VIII.β3 library at calculating the eigenvalue, and it is the most sensitive, exhibiting a difference of 103 pcm between the maximum and minimum variations. This specific benchmark has a very large uncertainty (490 pcm), and the ENDF/B-VIII.β3 and simulation results are both just outside this uncertainty threshold.

As a further check, the benchmark problems were also run with the ACE files from the 60 accepted ensembles. These plots are shown in Figure 19 for the PST benchmark, Figure 20 for the LCT benchmark, and Figure 21 for the HCT benchmark. In each of these plots, the first data point represents the benchmark, and the next 60 are the simulation runs. Of the 60 simulations, 8 runs did not finish due to MCNP losing track of the particles. These runs are shown as a red x equal to the arithmetic average of the other 52 runs.

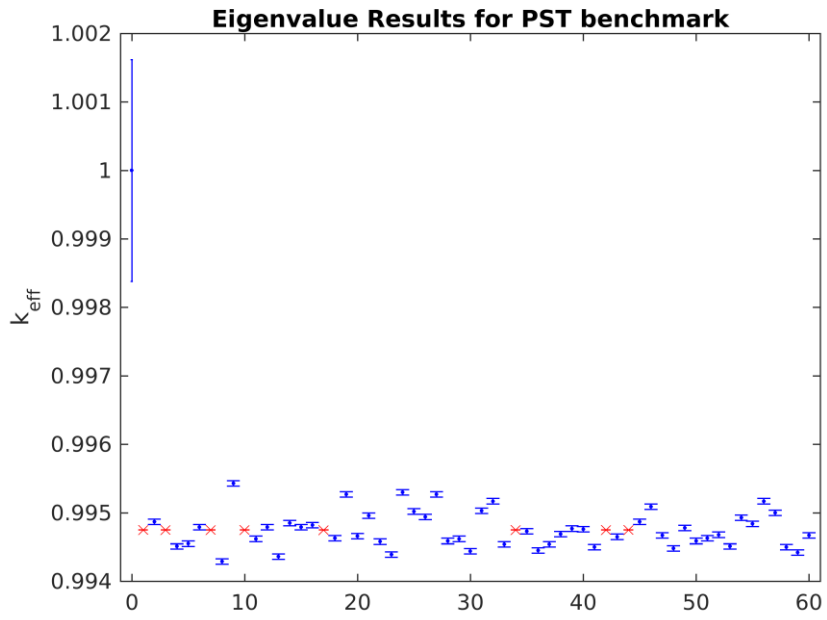


Figure 19. PST benchmark run for each accepted ensemble

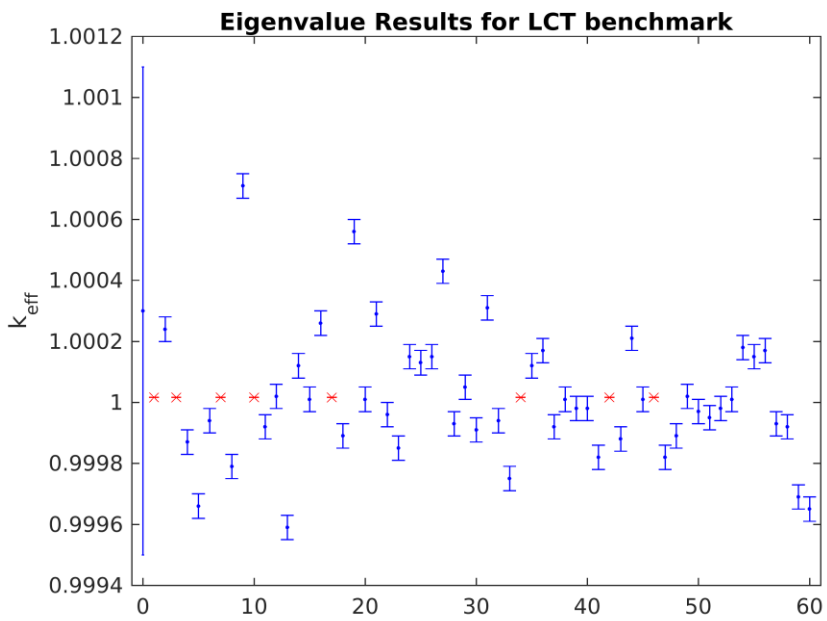


Figure 20. LCT PST benchmark run for each accepted ensemble

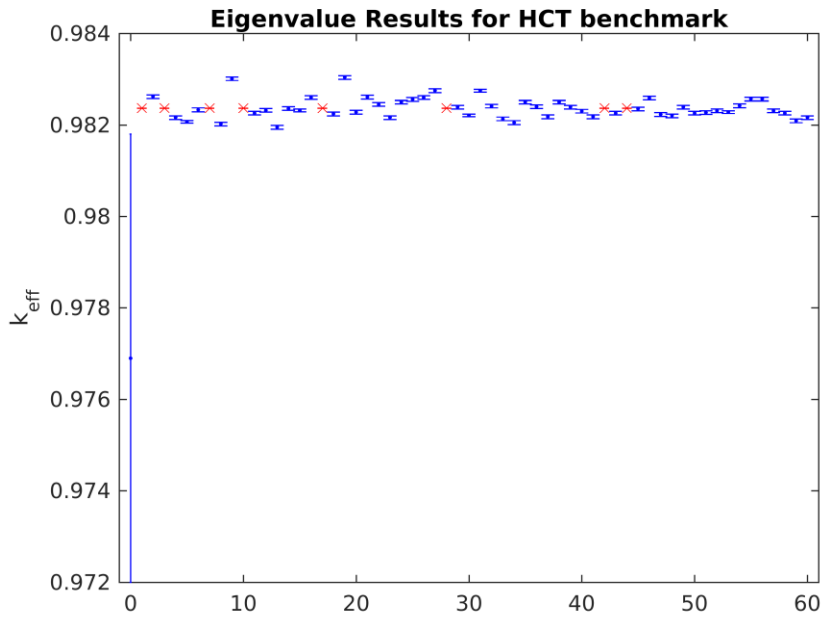


Figure 21. HCT PST benchmark run for each accepted ensemble

It is interesting that, even though all three of the benchmarks are remarkably different, the trends of the 52 simulations are remarkably similar. The difference between the maximum and minimum values of the PST, LCT, and HCT ensembles are 114, 112, and 109 pcm, respectively. These are much more closely packed together than the results from Table 10 to Table 12, which were 26, 78, and 103 pcm, respectively. This may indicate that the previous method of perturbing the DSF, adding the uncertainty times a Gaussian random number, is not a good way to evaluate the sensitivities.

CHAPTER 5. CONCLUSION AND FUTURE WORK

A new methodology for generating thermal neutron scattering kernels has been developed that combines information from experiments and computer simulations which evaluates not only thermal scattering kernels, but their associated uncertainties and covariance matrices. The application of the UMC method shows that, while previously only used in fast-spectrum data, it can be used for thermal scattering data. This is the first time thermal neutron DDCS were used in UMC calculations to fit atomic interaction parameters. The evaluated DDCS and total cross sections obtained in this way were found to be in good agreement with the ENDF/B-VII.1 and ENDF/B-VIII.β3 cross sections, but unlike the extant evaluations, the presented evaluation framework has quantified uncertainties of corresponding cross sections stemming from underlying atomic interaction parameters, and has enabled propagation of these uncertainties to simulations of integral benchmark experiments for the first time. The evaluated cross section generally showed improved performance in integral benchmark experiments over the ENDF/B-VII.1 and ENDF/B-VIII.β3 cross sections. Although the evaluated cross sections have performed as well as these extant evaluations, a more important contribution of this work was to quantify uncertainties in DSF and DDCS that originate from uncertainties in parameters of molecular dynamics model, and to quantify the corresponding uncertainty of in simulations of integral benchmark experiments.

While incoherent approximation used in this work is justified for water, other methods of evaluating the DSF, such as the Van Hove theory or various *ab initio* models can be used due to the generality of the evaluation framework. Since the Van Hove

theory is currently limited to being calculated after applying classical approximations, generating the atomic trajectories using more accurate molecular dynamics methods (such as *ab initio* molecular dynamics) are expected to yield more accurate results. There has been a recent attempt to combine the Gaussian approximation with the Van Hove theory [35], which could be expanded to include coherent contributions.

This work presents a Monte-Carlo estimate of sensitivities of several integral benchmark experiments to uncertainties in thermal neutron scattering kernel. This is the first step in addressing the absence of methods of propagating thermal neutron scattering covariance data through neutron transport codes and the related calculation of sensitivities of integral benchmark experiments to thermal neutron scattering data. It is hoped that this work will encourage development of other innovative methods for generating thermal scattering data and its covariance. While the framework allows for the construction of a covariance matrix, one was not calculated in this current implementation, and will be included in future publications. The presented framework can be applied to any material, including other materials of interest for thermal reactor applications (such as graphite, Silicon Carbide, or FLiBe), as well as materials important for criticality safety applications (such as lucite, Teflon, and polyethylene).

APPENDIX A DOUBLE DIFFERENTIAL CROSS SECTION PLOTS

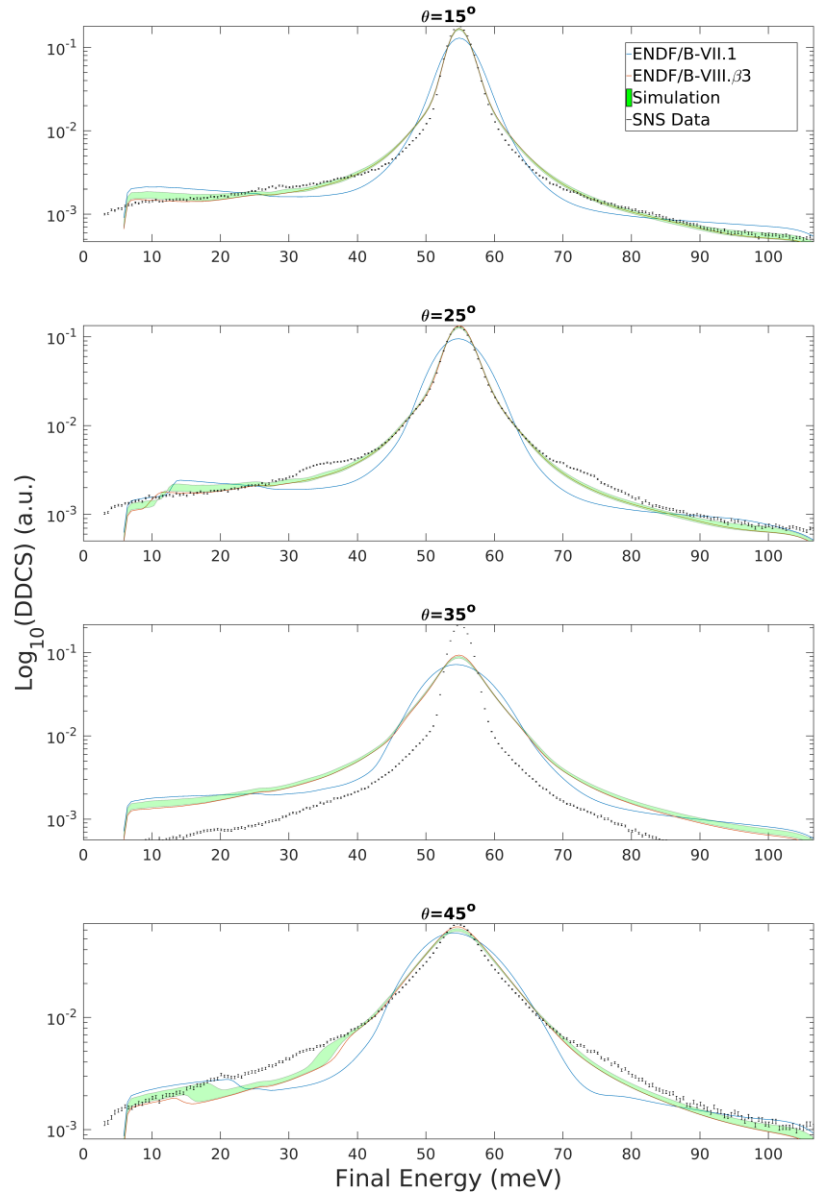


Figure 22: SNS DDCS plots for $E_i=55$ meV

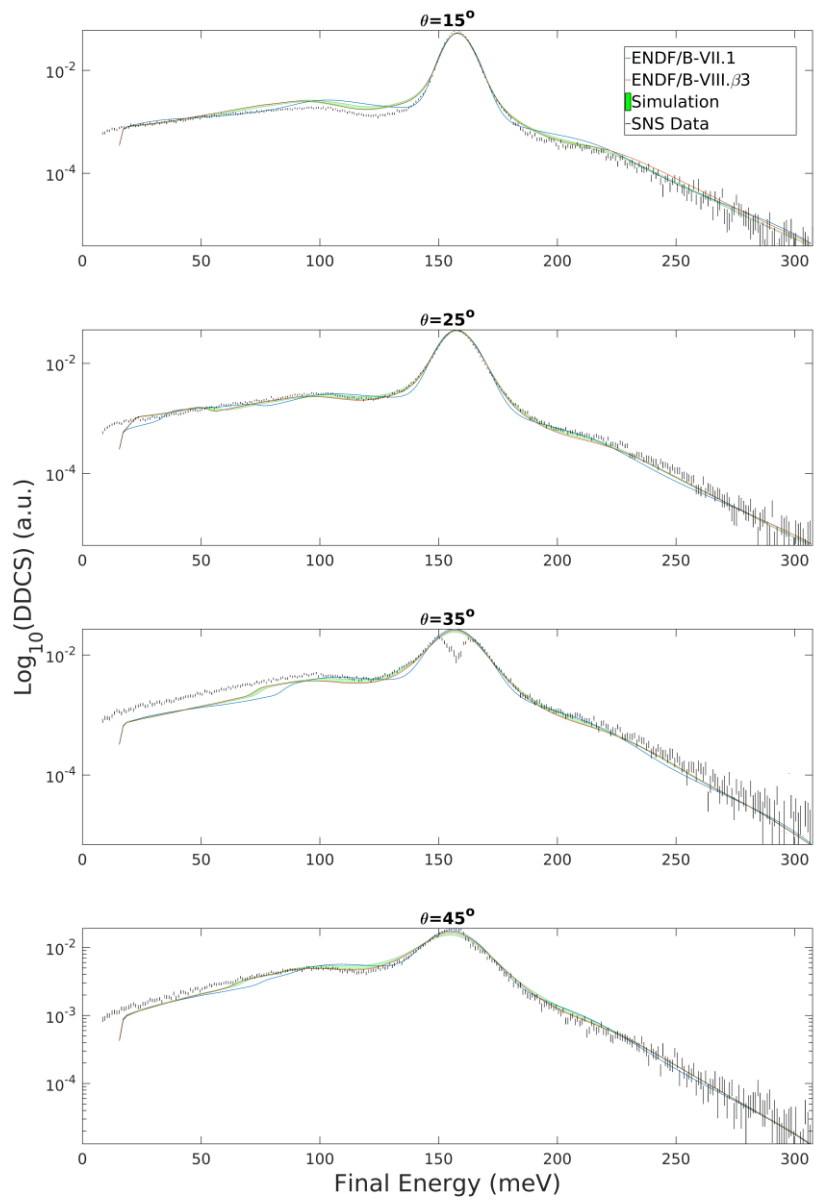


Figure 23: SNS DDCS plots for $E_i=160$ meV

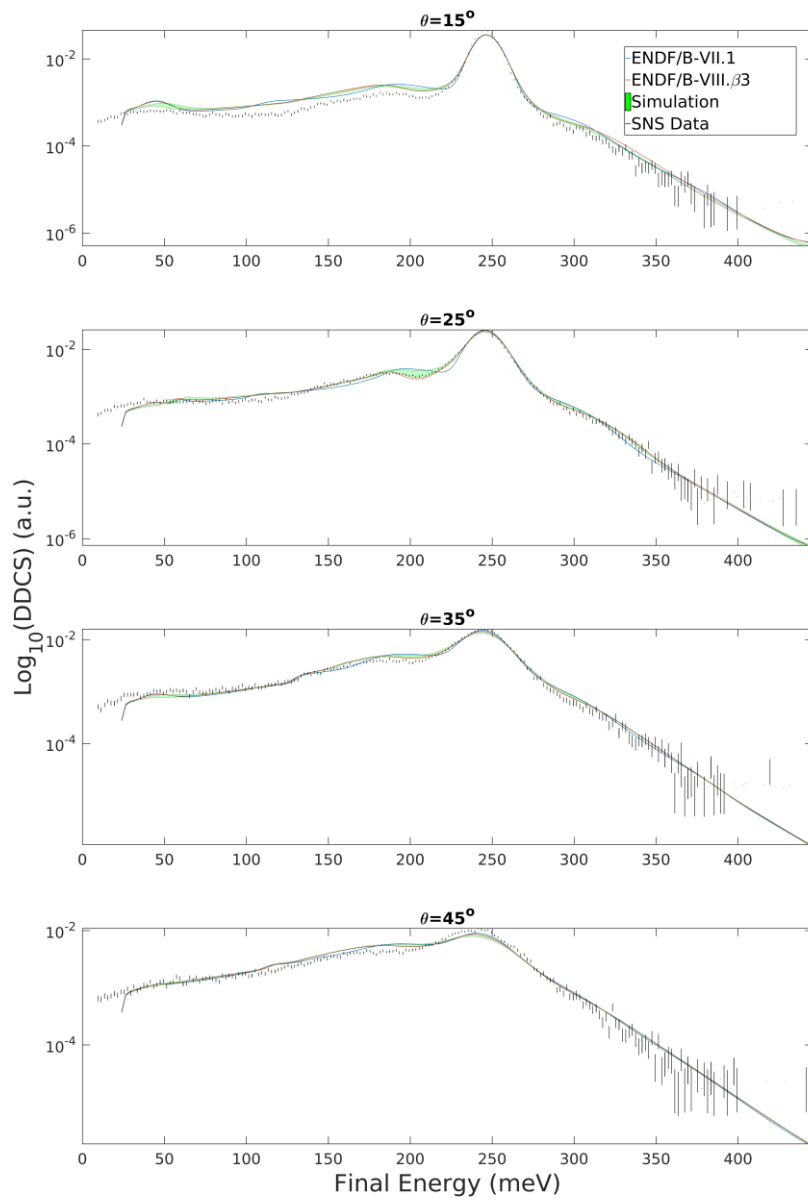


Figure 24: SNS DDCS plots for $E_i=250$ meV

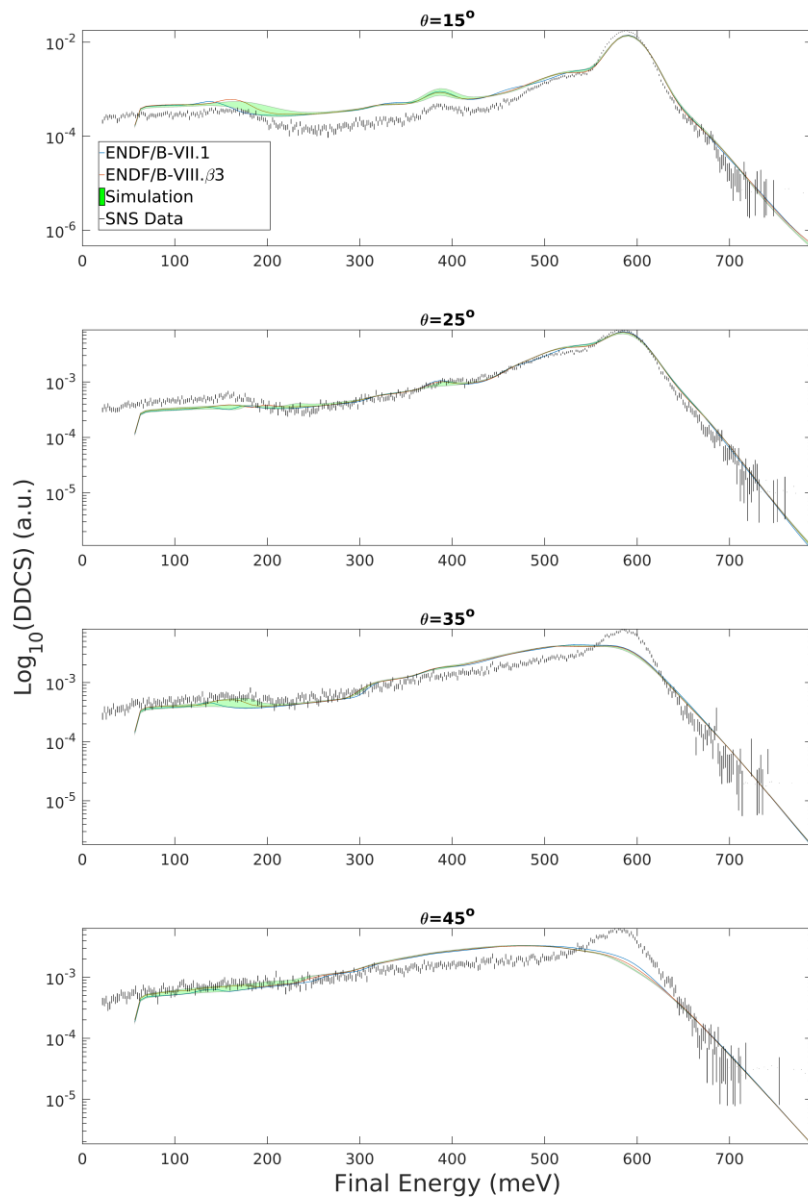


Figure 25: SNS DDCS plots for $E_i=600$ meV

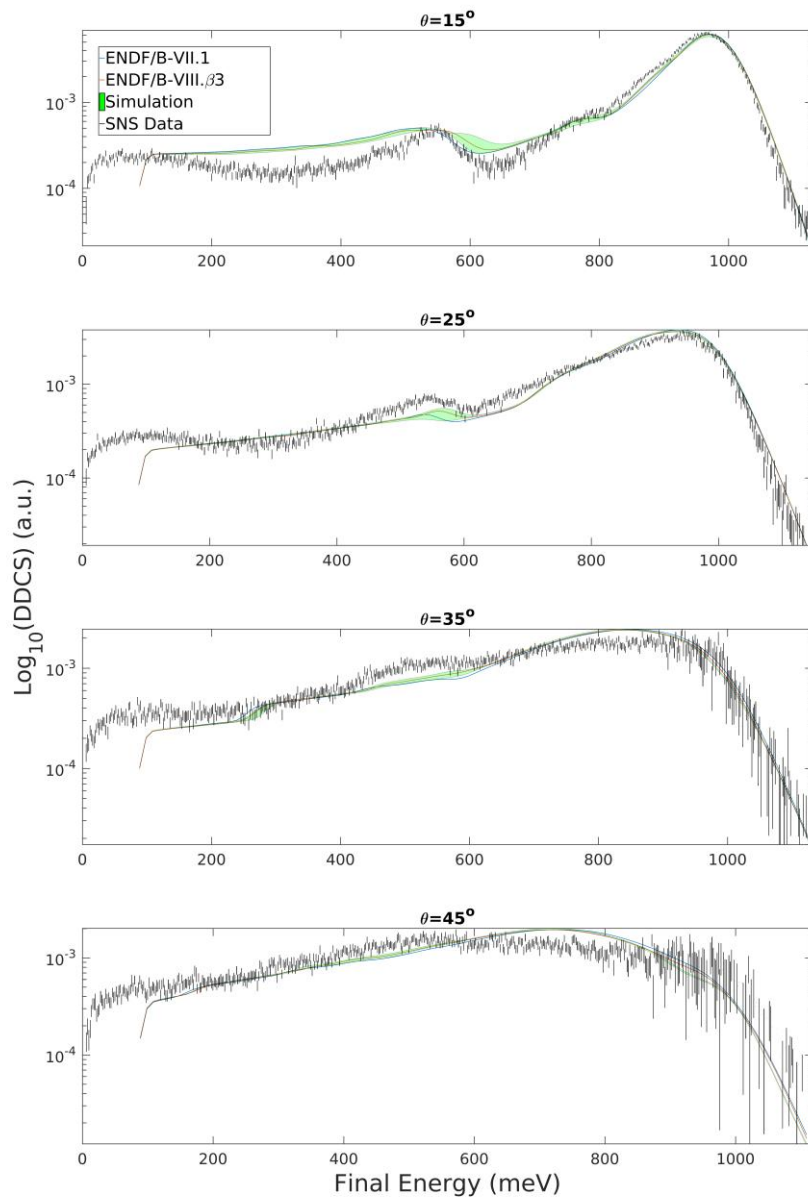


Figure 26: SNS DDCS plots for $E_i=1000$ meV

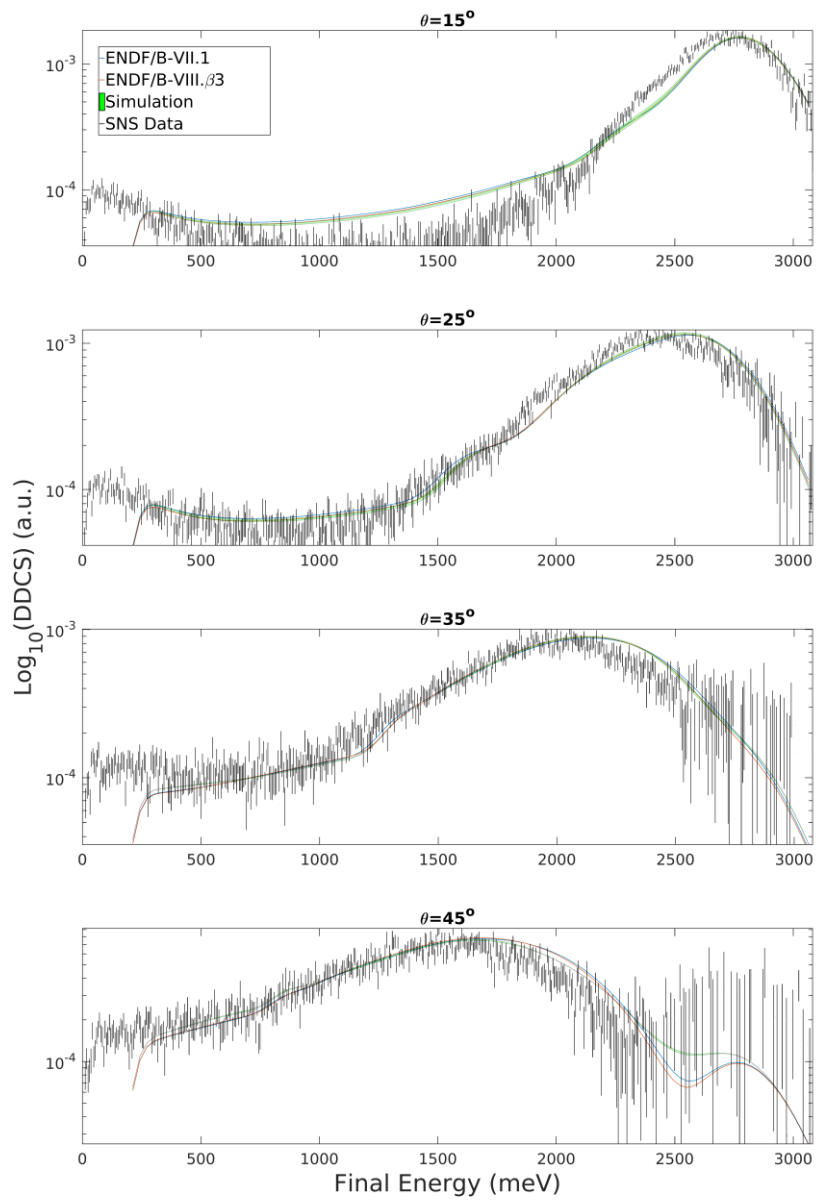


Figure 27: SNS DDCS plots for $E_i=3000$ meV

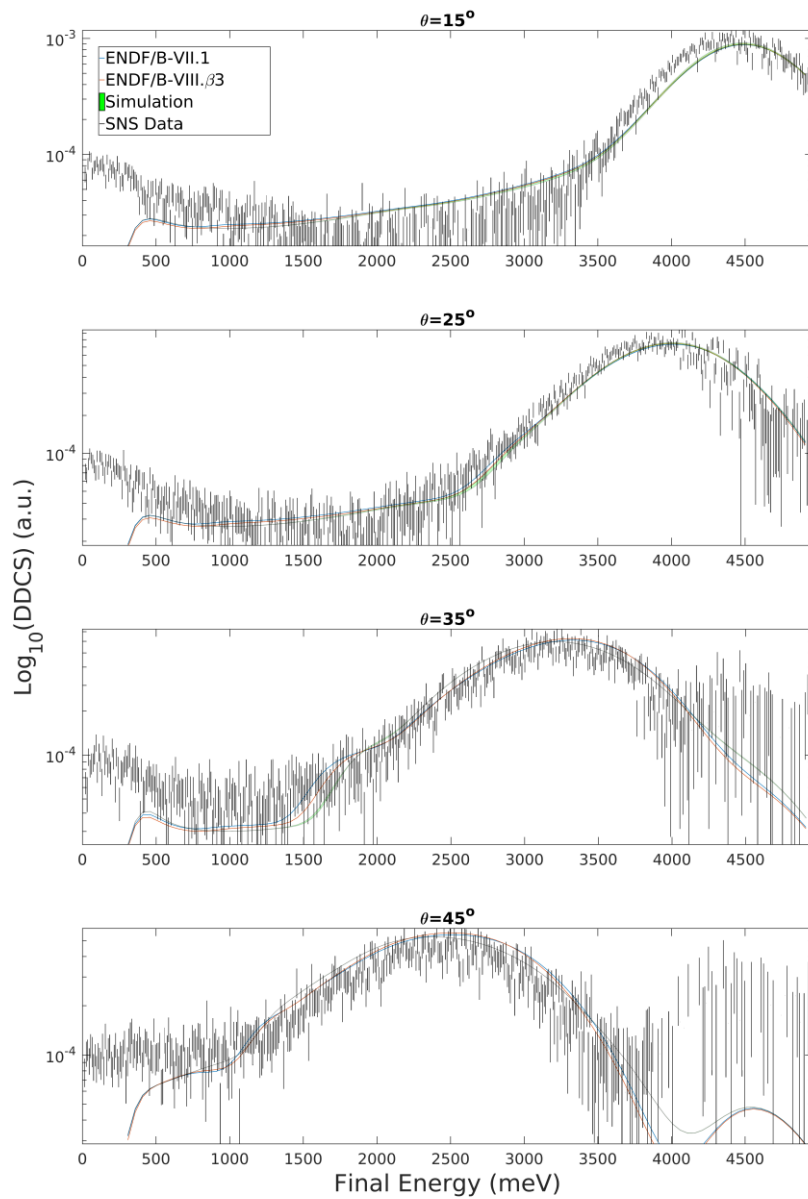


Figure 28: SNS DDCS plots for $E_i=5000$ meV

REFERENCES

- [1] D. E. Cullen, R. N. Blomquist, C. Dean, D. Heinrichs, M. A. Kalugin, M. Lee, Y. Lee, R. MacFarlane, Y. Nagaya and A. Trkov, "How Accurately Can We Calculate Thermal Systems?," Livermore (CA): Lawrence Livermore National Laboratory (Report UCRL-TR-203892), 2004.

- [2] J. C. Holmes, A. I. Hawari and M. L. Zerkle, "A Phonon-based Covariance Methodology for ENDF S(alpha,beta) and Thermal Neutron Inelastic Scattering Cross Section," *Nuclear Science and Engineering*, vol. 184, pp. 84-113, 2016.

- [3] B. Guillot, "A Reappraisal of What We Have Learnt During Three Decades of Computer Simulations of Water," *Journal of Molecular Liquid*, vol. 101, pp. 219-260, 2002.

- [4] J. F. Ouyang and R. P. A. Bettens, "Modelling Water: A Lifetime Enigma," *Chimia*, vol. 69, pp. 104-111, 2015.

- [5] M. S. Nelkin, "Scattering of Slow Neutrons by Water," *Physical Review*, vol. 119, no. 2, pp. 741-746, 1960.

- [6] J. Koppel and D. H. Houston, "Reference Manual for ENDF Thermal Neutron Scattering Data," General Atomic report GA-8774 revised and reissued as ENDF-

269 by the National Nuclear Data Center, July 1978.

- [7] R. MacFarlane, "New Thermal Neutron Scattering Files for ENDF/B-VI, Release 2," LA-12639-MS (ENDF-356), March 1994.

- [8] R. E. MacFarlane and D. W. Muir, "The NJOY Nuclear Data Processing System," LA-12740-M, 1994.

- [9] M. Mattes and J. Keinert, "Thermal Neutron Scattering Data for the Moderator Materials H₂O, D₂O, and ZrHx in ENDF-6 Format and as ACE Library for MCNP(X) Codes," INDC/NDS, 2005.

- [10] J. Marquez Damian, J. Granada and D. Malaspina, "CAB models for water: A new evaluation of the thermal neutron scattering laws for light and heavy water in ENDF-6 format," *Annals of Nuclear Energy*, vol. 65, pp. 280-289, 2014.

- [11] G. L. Squires, *Thermal Neutron Scattering*, Cambridge: Cambridge University Press, 1978.

- [12] D. L. Price and F. Fernandez-Alonso, "Chapter 1 - An Introduction to Neutron Scattering," in *Experimental Methods in Physics - Volume 44*, Academic Press, 2013, pp. 1-136.

- [13] K. Gottfried and T. Yan, *Quantum Mechanics: Fundamentals*, New York: Springer, 2003.
- [14] L. V. Hove, "Correlations in Space and Time and Born Approximation Scattering in Systems of Interacting Particles," *Physics Review*, vol. 95, no. 1, pp. 249-262, 1954.
- [15] P. Schofield, "Space-Time Correlation Function Formalism for Slow Neutron Scattering," *Physics Review Letters*, vol. 4, no. 5, pp. 239-240, 1960.
- [16] P. Egelstaff, "Neutron Scattering Studies of Liquid Diffusion," *Advances in Physics*, vol. 11, no. 43, pp. 203-232, 1962.
- [17] B. J. Berne and G. D. Harp, "On The Calculation of Time Correlation Functions," *Advance in Chemical Physics*, vol. 17, pp. 63-227, 1970.
- [18] G. R. Kneller, "Inelastic neutron scattering from classical systems - Stationary phase approximation of the scattering law," *Molecular Physics*, vol. 83, no. 1, pp. 63-87, 1994.
- [19] I. I. Gurevich and L. V. Tarasov, *Low-Energy Neutron Physics*, Amsterdam: North-Holland, 1968.
- [20] F. H. Frohner, "Evaluation and Analysis of Nuclear Resonance Data," JEFF Report

18, 2000.

- [21] R. Capote and D. L. Smith, "An Investigation of the Performance of the Unified Monte Carlo Method of Neutron Cross Section Data Evaluation," *Nuclear Data Sheets*, vol. 109, pp. 2768-2773, 2008.
- [22] D. Smith, *Probability, Statistics, and Data Uncertainties in Nuclear Science and Technology*, LaGrange Park, IL: American Nuclear Society, 1991.
- [23] R. Capote, D. Smith, A. Trkov and M. Meghzifene, "A new formulation of the Unified Monte Carlo approach (UMC-B), and cross-section evaluation for the dosimetry reaction $^{55}\text{Mn}(n,\gamma)^{56}\text{Mn}$," *Journal of ASTM International*, vol. 9, 2012.
- [24] T. Darden, D. York and L. Pedersen, "Particle mesh Ewald: An $N\log(N)$ method for Ewald sums in large systems," *Journal of Chemical Physics*, vol. 98, no. 12, p. 10089, 1993.
- [25] D. Van Der Spoel, E. Lindahl, B. Hess, G. Groenhof, A. Mark and H. Berendsen, "GROMACS: Fast, flexible, and free," *Journal of Computational Chemistry*, vol. 26, no. 16, pp. 1701-1718, 2005.
- [26] M. Gonzalez and J. Agascal, "A flexible model for water based on TIP4P/2005," *The Journal of Chemical Physics*, vol. 135, 2011.

- [27] E. Farhi, G. Ferran, W. Haeck, E. Pellegrini and Y. Calzavara, "Light and heavy water dynamic structure factor for neutron transport codes," *Journal of Nuclear Science and Technology*, vol. 52, no. 6, 2014.
- [28] W. L. Jorgensen, J. Chandrasekhar, J. D. Madura, R. W. Impey and M. L. Klein, "Comparison of Simple Potential Functions for Simulating Liquid Water," *Journal of Chemical Physics*, vol. 79, pp. 926-935, 1983.
- [29] O. K. Harling, "Slow Neutron Inelastic Scattering Study of Light Water and Ice," *The Journal of Chemical Physics*, vol. 50, pp. 5279-5296, 1969.
- [30] N. Otuka, E. Dupont, Semkova, V. and e. al., "Towards a More Complete and Accurate Experimental Nuclear Reaction Data Library (EXFOR): International Collaboration Between Nuclear Reaction Data Centres (NRDC)," *Nuclear Data Sheets*, vol. 120, pp. 272-276, 2014.
- [31] K. Zaitsev, V. Petrov, S. Kuznetsov, O. Langer, I. Meshkov and A. Perekrestenko, "The total cross sections of the interaction of ultracold neutrons with H₂O and D₂O," *Atomic Energy*, vol. 70, pp. 238-242, 1991.
- [32] "International Handbook of Evaluated Criticality Safety Benchmark Experiments," NEA/NSC/DOC(95)03/I-VII, Organization for Economic Co-operation and Development Nuclear, Sep. 2010.

- [33] A. Nouri, P. Nagel, J. Briggs and T. Ivanova, "DICE: Database for the International Criticality Safety Benchmark Evaluation Program Handbook," *Nuclear Science and Engineering*, vol. 145, no. 11, 2003.
- [34] "SCALE: A Modular Code System for Performing Standardized Computer Analyses for Licensing Evaluation, " *ORNL/TM-2005/39, Version 6, Vols. I-III, Oak Ridge National Laboratory, Oak Ridge, Tennessee, January 2009.*, Available from Radiation Safety Information Computational Center at Oak Ridge National Laboratory as CCC-750..
- [35] Y. Abe and S. Tasaki, "Molecular dynamics analysis of incoherent neutron scattering from light water via the Van Hove space–time self-correlation function with a new quantum correction," *Annals of Nuclear Engineering*, vol. 83, pp. 302-308, 2015.